https://doi.org/10.5194/egusphere-2026-4286
Preprint. Discussion started: 31 July 2026

Airborne Lidar measurements of wind profiles during the MAGIC-2021 campaign

Nicolas Cézard[1], Matthieu Valla[2], Laurent Lombard[2], Béatrice Augere[2], Julien Lahyani[2], William Patiño-Rosas[2], Didier Goular[2], Christophe Planchat[2], Agnès Dolfi-Bouteyre[2], Anne Durecu[2], François Gustave[2], Anasthase Liméry[2], Mathieu Quatrevalet[3], Elias Wolkiewiez[4], Cyril Crevoisier[4]

[1] ONERA/DOTA, Université de Toulouse, F- 31055 Toulouse, France
[2] ONERA/DOTA, Université de Paris-Saclay, F- 91120 Palaiseau, France
[3] DLR/IPA, 82234 Oberpfaffenhofen, Germany
[4] LMD/IPSL, CNRS, Ecole polytechnique, F-91128 Palaiseau, France

Correspondence to: Nicolas Cézard (nicolas.cezard@onera.fr)

Abstract. Wind is an essential physical variable in atmospheric physics, and airborne Doppler lidars are valuable tools for profiling wind fields over wide areas. The paper reports on wind measurements performed with an airborne 1.5 µm coherent Doppler Lidar, during a campaign called MAGIC (*Monitoring of Atmospheric composition and Greenhouse gases through multi-Instrument Campaigns*) that took place in summer 2021 in France and in the Arctic. Vertical profiles of the horizontal wind (*u* and *v* components) are obtained with 150 m vertical resolution and a typical horizontal resolution of 2.5 km. Continuous wind profiling capability over vertical ranges up to 7.5 km is demonstrated. Two wind products are derived and compared, depending of the method used to correct for the aircraft speed. LGE-based wind product (Lidar Ground Echo) derives the aircraft speed from the Doppler shift measured by the lidar on the ground surface. FTI-based wind product (Flight Test Instrumentation) uses aircraft speed measurements by the navigation instruments. Through examples of lidar measurements realized during the campaign, advantages and limitations of LGE-based and FTI-based wind profiles are discussed. The LGE technique performs better over land and under clear weather, but the FTI technique, being independent of ground visibility and surface nature, is more generally usable. Yet it is found to exhibit some excess noise in the range of +0.6 to +0.8 $m.s^{-1}$ in standard deviation along zonal and meridional wind components, attributed to aircraft random vibrations. Lidar wind profiles are compared to radiosonde measurements and are shown to agree within an average standard deviation of 1.2 $m.s^{-1}$ in magnitude, over three datasets. They are also compared with independent wind data provided by the ECMWF Integrated Forecast System (IFS cycle 41r2). Both data sets agree within residual standard deviations in the range of 1.3-2 $m.s^{-1}$ for zonal and meridional components, over six different flights (~21 hours of measurements). This airborne lidar appears as a promising tool for future scientific campaigns dedicated to climate modelling and atmospheric dynamics.

https://doi.org/10.5194/egusphere-2026-4286
Preprint. Discussion started: 31 July 2026

1. Introduction

Wind is identified as an Essential Climate Variable in the Global Climate Observing System (GCOS, 2022) of the World Meteorological Organization. Its knowledge is crucial in many research fields, like weather forecast, turbulent processes studies, or greenhouse gas flux measurements to name a few. Among the available instruments for measuring wind, Coherent Doppler Lidars (CDL) feature attractive properties. They offer remote sensing capability, and compared to Doppler radars, they are sensitive to much smaller atmospheric particles, with sizes in the order of magnitude of the laser wavelength. This enables them to conduct range-resolved measurements in optically-thin aerosol layers. Wind values are derived from the Doppler frequency shift of the laser light backscattered by the atmospheric aerosols, used as wind tracers. CDL perform generally very well in the bottom layers of the atmosphere, often significantly loaded with aerosols. They are therefore commonly used nowadays as ground-based remote sensors. Nevertheless, when it comes to evaluate atmospheric dynamics in extended areas, especially over hardly accessible places (oceans, deserts, mountains, remote lands…), airborne wind measurements become highly desirable. A recent comprehensive review of airborne wind lidars has been published recently (Yew et al., 2025), illustrating the diversity of research activities conducted with such systems. The review also evidences that a large majority of airborne wind lidars reported in the last decade are infrared CDL at 1.5 µm or 2 µm. Infrared CDL technology benefits indeed of numerous fiber-based and integrated components, which makes it easier to implement into an aircraft than other wind lidar technologies, such as visible or ultra-violet direct-detection lidars. In the two last decades, only a few successful developments of airborne CDL for vertical profiling of wind over long ranges (> km) have been reported, mainly in USA (Schroeder et al., 2020; Kavaya et al., 2014), China (Zhang et al., 2024; Liu et al., 2016), Germany (Weissmann et al., 2005; Witschas et al., 2017), and France (Augere et al., 2019). This paper deals with this latter development.

In 2019, we reported indeed on a new airborne 1.5 µm CDL named LIVE (for Lidar Vent, french for Wind Lidar), designed to measure vertical profiles of the wind vector, downward-looking from an aircraft. The lidar had been tested during two short flights onboard an ATR-42 operated by SAFIRE, the French facility for airborne scientific research. The 2019 campaign was unfortunately too short to conduct a thorough evaluation of the lidar capabilities. A calibration issue also imposed relying exclusively on the Lidar Ground Echo technique (detailed below) to subtract the aircraft groundspeed from the velocity Doppler profiles, a method that can be used only over solid ground and in clear weather conditions, as we shall see hereunder. There was thus room for improvements but the lidar potential was encouraging. By the end of 2019, LIVE was therefore selected to integrate a larger-scale scientific campaign called MAGIC (*Monitoring of Atmospheric composition and Greenhouse gases through multi-Instrument Campaigns*), planned for 2021, and referred to in this paper as MAGIC-2021.

The French Laboratoire de Méteorologie Dynamique (LMD) and CNES space agency started organizing MAGIC campaigns in 2018 (Crevoisier, 2018). As the name indicates, these campaigns mainly target Greenhouse Gas (GHG) measurements, and usually feature in situ and remote sensors operated from a variety of platforms (ground-based, airborne, balloon-borne,

https://doi.org/10.5194/egusphere-2026-4286
Preprint. Discussion started: 31 July 2026

satellites). The target area for the MAGIC-2021 campaign was northern Scandinavia. The region is known to be rich of potential CH_4 and CO_2 hotspots (wetlands, peat bogs, oil & gas platforms) while suffering from a lack of measurements from ground stations and satellite remote sensors. In the context of GHG studies, accurate wind field data were identified as highly desirable for constraining dispersion and transport models. Furthermore, if wind measurements could be co-located in time and space with gas measurements, especially in the planetary boundary layer (PBL), it could open the way for direct evaluation of local GHG surface fluxes (Wolff et al. 2021, Krautwurst et al. 2025). For MAGIC-2021, it was thus decided to set a double-lidar airborne payload, composed of DLR's CH_4/CO_2 lidar named CHARM-F (Amediek et al. 2017), and of ONERA's wind lidar LIVE. The main scientific objective for the Doppler lidar was to deliver vertical profiles of horizontal winds (u and v components, or modulus and direction), down to the PBL if possible. Both lidars were installed in the ATR-42 operated by SAFIRE, and the campaign took place as scheduled in August 2021 (Crevoisier, 2021). It gathered 17 research teams from seven different countries, and involved a large amount and variety of sensors, operated from ground, balloons launched from Esrange station (Sweden) and research aircrafts based in Kiruna airport (Sweden). The campaign research area extended over northern Sweden, Finland and Norway, with also preliminary flights in France.

During the campaign, despite adverse weather conditions, more than 20 hours of measurements have been carried out by the airborne lidar LIVE, during six different flights. This provided a far more exhaustive database than in 2019 to evaluate the lidar performances over dry land and sea surfaces, from various flight altitudes (from 5 to 8 km), and under mixed clear/cloudy weather conditions. Because of frequent clouds during the arctic flights, and several sequences over sea, it was also not possible to rely only on the Lidar Ground Echo (LGE) technique to subtract the aircraft groundspeed from the velocity Doppler profiles, as was done in 2019. We have therefore implemented a more suitable technique relying on groundspeed measurements given by the aircraft Flight Test Instrumentation (FTI), i.e. a GPS. This well-known solution allows retrieving wind profiles down to the clouds even without ground visibility, and over sea. Yet it requires a careful calibration of the lidar frame within the aircraft, and it is more sensitive than the LGE technique to aircraft attitude angle changes and vibrations. The MAGIC-2021 campaign made possible to compare both techniques and quantify the excess noise of the FTI-based wind profiles with respect to LGE-based wind profiles, a study that we have not seen elsewhere to the best of our knowledge. The campaign also permitted to conduct a quantitative validation of the lidar measurements, through comparison with radiosondes measurements. Finally, the lidar profiles could also be compared with simulated wind fields computed from the European Centre for Medium-Range Weather Forecasts (ECMWF) ERA5 database. The goal of this paper is to present these new results and show wind profiles measurement examples, thereby establishing a clear view of the airborne lidar performances.

https://doi.org/10.5194/egusphere-2026-4286
Preprint. Discussion started: 31 July 2026

2. Material and methods

2.1 Lidar instrument

A detailed technical description of the CDL Lidar LIVE can be found in Augere et al. (2019). In this section, we only recall the main lidar parameters, and explain how they relate to the lidar performance and to wind profiles properties. LIVE features an all-fiber, 1.5 µm laser source developed and built at ONERA. For the MAGIC-2021 campaign, the pulse energy, duration, and repetition frequency (PRF) were set to $E_P = 420$ µJ, $\tau_P = 1$ µs, and PRF = 14 kHz respectively. The PRF determines the lidar ambiguity range, above which lidar echoes from consecutive pulses start to overlap. This range is given by $d_{amb} = c/(2*PRF)$, with c the speed of light, and equals 10.7 km for LIVE. This was enough for the campaign, since the aircraft flight altitude always remained below 9 km, and the nominal emission angle with respect to nadir was limited to 15°.
The pulse duration determines the minimal vertical resolution of the measurement, according to $\Delta z_{min} \approx c\,\tau_P/2$=150 m. All the results in this paper are displayed with this resolution. The pulse duration and shape also determine the length of the lidar measurement blind zones, located below the aircraft and above Strongly Scattering Objects (SSO) such as ground, sea, thick clouds, etc. This is a typical effect encountered with many lidars. When a laser pulse is transmitted to the atmosphere, light backscattered by the pulse trailing edge on the aircraft window overrides the signal backscattered by the rest of the pulse from nearby aerosols, as both arrive at the same time on the detector. The same phenomenon occurs in a time-reversed way when the laser pulse encounters an SSO. For this reason, LIVE cannot deliver wind data just below the aircraft and just above SSO, within blind zones extending typically along $\Delta z_{blind} = 2\Delta z_{min}$, i.e. 300 m. The factor 2 comes from the fact that the backscattering ratio between SSO and aerosols is so high that pulse tails must be also considered. These blind zones could thus be reduced in the future by shortening pulse duration or steepening pulse tails.
The pulse energy drives both the range and accuracy of the measurements. The higher the better, but several factors limit pulse energy: physical factors (for instance, detrimental non-linear effects occur in fibers above some peak-power threshold) and practical factors (the overall laser complexity increases with laser power, decreasing its suitability for airborne operation). For LIVE, the chosen combination of pulse energy, duration, and PRF resulted from a careful tradeoff between performance and suitability for an airborne environment.

The laser unit is connected to a 10 cm diameter telescope, that expands the laser beam and transmits it to a motorized scanner system. The scanner pattern can be parameterized at will for a given scientific purpose. For the MAGIC-2021 campaign, it was set to perform a full scanning pattern in 21 seconds, comprising 17 seconds for a 360° continuous conical scan of full-angle aperture θ = 30°, 2 seconds for a fixed-axis emission along the cone axis (i.e. lidar-relative nadir), and 2 seconds for motor motion in between. The 21 seconds period determines the horizontal lidar sampling rate. Given the typical aircraft speed with respect to the ground (80-120 m.s^{-1}), this sampling rate was in the range of 1.7-2.5 km. Since the aircraft is moving while

https://doi.org/10.5194/egusphere-2026-4286
Preprint. Discussion started: 31 July 2026

scanning, the cone pattern projected on ground is not circular, but rather draws cycloidal loops. An example is shown in Figure 1. The lidar spatial resolution, across-track and along-track, can be defined as the loop size at ground level. The exact shape and size of these loops vary during the flight, as they depend on numerous parameters such as the aircraft groundspeed, flight altitude, or sideslip, pitch and roll angles. In the simplest case (sideslip, pitch and roll angles all null), the across-track lidar resolution is given by $z.sin\theta$, where z is the ground-relative flight altitude. The along-track resolution is a more complex, but computable, function of flight altitude and aircraft groundspeed. At a typical groundspeed of 100 $m.s^{-1}$ and z=5000 m, the lidar sampling distance is 2.1 km, the along-track resolution 1.8 km, and the across-track resolution 2.5 km.

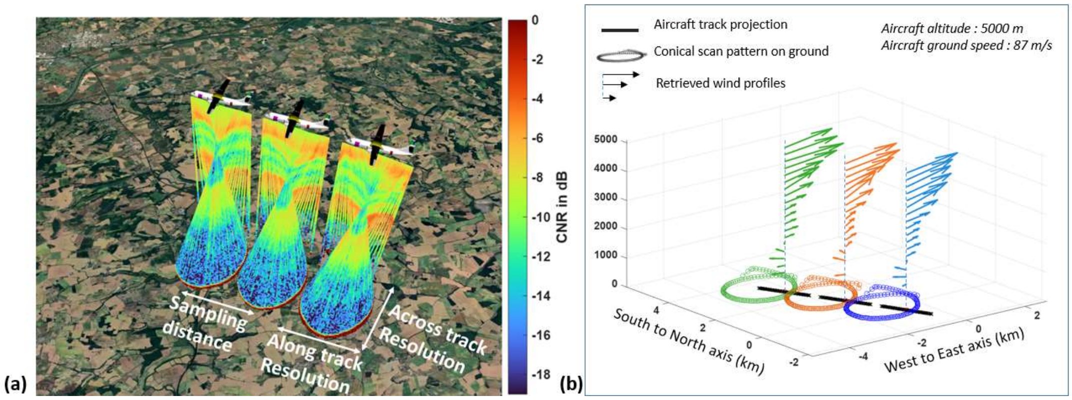

Figure 1. (a) Atmospheric lidar signals recorded during three consecutive conical scans (11/08/2021, 12:29 UTC, France). Cone0 colors correspond to line-of-sight Carrier-to-Noise Ratio (CNR). Map data © Google, © Airbus 2026. All rights reserved; (b) Corresponding scan patterns projected on ground, and retrieved wind profiles for each cone. For clarity, only wind data above 700 m are shown, with a degraded 240 m sampling rate. Arrow lengths are upscaled by a factor of 100. The frame origin is arbitrarily positioned at the first point of the blue scan projection.

From a practical point of view, the entire lidar weights 85 kg, and its degree of automation is high enough for a single operator to use it. Real-time displays of the lidar signal power and so-called radial velocity (i.e. aerosol velocity relative to the lidar and projected onto the laser line-of-sight (LOS)), are provided onboard at 10 Hz rate. This allows the operator to verify that the lidar is operating correctly, and also to assess aerosol load conditions in order to optimize the flight in real-time, whenever possible. For instance, if the atmosphere looks pristine (low backscattered signal), the decision can be made to decrease flight altitude to reduce the range and enhance signal power. Conversely if strong aerosol backscattering is observed, flight altitude can be increased to extend lidar coverage. For the MAGIC-2021 campaign, all the lidar traces were recorded and stored in full waveform during the flight, involving a data volume of 0.77 $To.hour^{-1}$. Several hard drives were available, and each one could

https://doi.org/10.5194/egusphere-2026-4286
Preprint. Discussion started: 31 July 2026

record a full ATR-42 flight without change. After landing, data were transferred to another storage space for processing and measurement products computation.

2.2. Measurement products

As illustrated in Figure 1b, the main output product of the CDL lidar LIVE is wind vector vertical profile. Two versions of this product are provided, depending of the used data source for measuring and subtracting the aircraft groundspeed from air velocity measurements: LGE-based wind profiles use the Lidar Ground Echo, and FTI-based wind profiles use data from the aircraft Flight Test Instrumentation (GPS data). As vectors, wind products are attached to a given framework. For winds we use the right-handed Cartesian geographic north-east-down (NED) coordinate system, also referred to as the "Earth frame" in this paper. A useful secondary output product is the lidar Carrier-to-Noise Ratio (CNR). The CNR is frequently used by CDL users as a quality indicator of the lidar measurement. It is also proportional to the atmospheric backscattering coefficient β in $m^{-1}.sr^{-1}$ (Fujii, 2005), thereby providing insights about the structure of atmospheric aerosol layers. It is a scalar field (independent of the framework), that can be mathematically defined in several ways. Here it is defined as the narrow-band CNR within a physical bandwidth of 7.8 MHz, which is approximately the frequency band occupied by the detected lidar signal. Figure **2** illustrates the way measurement products are derived from the lidar data and ancillary data. It also introduces the three frameworks, and framework rotation operations, that will be discussed later on. The aircraft frame is defined as the right-handed cartesian nose/right-wing/nadir coordinate system. The lidar frame is defined as the aircraft frame rotated by small angles (determined in Sect.2.3) along the three aircraft axes.

https://doi.org/10.5194/egusphere-2026-4286
Preprint. Discussion started: 31 July 2026

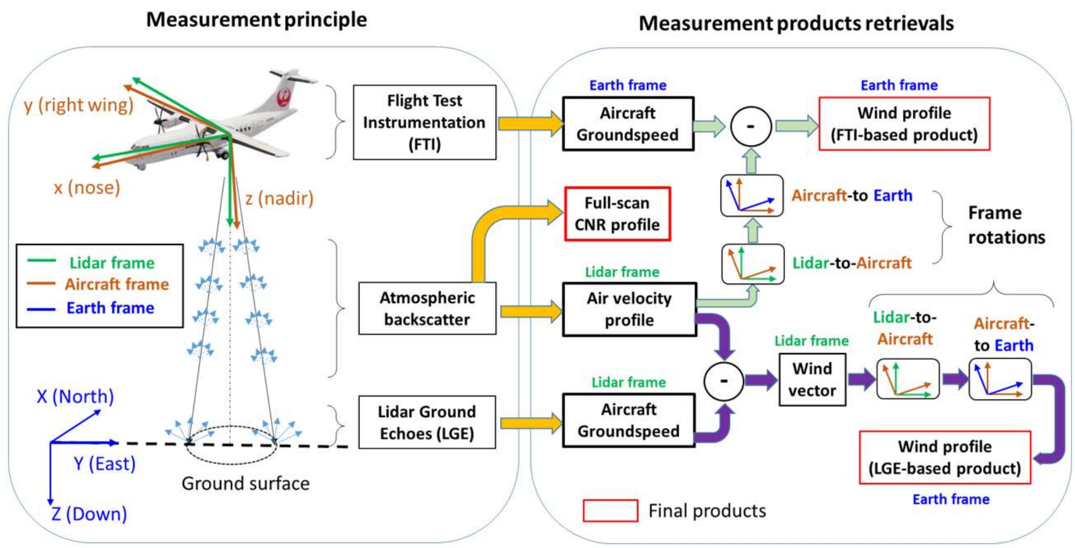

Figure 2. Schematic of the measurement principle (left) and computation of wind fields and CNR retrievals (right). Green, brown and blue texts indicate the framework attached to the different vector fields.

The wind profile computation comes essentially in two steps. The first one is the air velocity profile calculation. In this paper, the terms “velocity” and “wind” designate respectively the airflow speed relative to the airborne lidar, and the airflow speed relative to the ground. Raw lidar data received from atmospheric backscatter are first grouped into consecutive packets of about 240 000 pulses, recorded during each 17 seconds conical scan (pulses recorded during the 4 remaining seconds between two scans are not exploited in this work). A velocity-vector vertical profile is then derived from this data packet, using an algorithm detailed in Augere et al. (2019). In short, for each range gate the algorithm relies on a VAD (Velocity Azimuth Display) fitting procedure of the sinewave pattern, drawn by the air velocity Doppler shift as a function of the cone scanning angle (Browning and Wexler, 1968). Moreover, when the signal is very low, an MFAS (Maximum Function of Accumulated Spectra) algorithm is used to infer the correct sinewave pattern, otherwise noise-flooded, and initiate a WVML estimator (Wind Vector Maximum Likelihood) that estimates the cone-averaged CNR and velocity vector components for the range gate. These techniques originate from and are detailed into a paper by Smalikho (2003). In our implementation, the output velocity-vectors and cone-averaged CNR profiles come with a vertical sampling of 38 m, meaning an oversampling factor of 4 with respect to the instrumental 150 m vertical resolution. The algorithm currently shows two main limitations. First, it works well only if the lidar LOS describes a regular cone in space during the measurement. Therefore, the algorithm is set to deliver *nan* data (not-a-number) when the aircraft roll, pitch or yaw angles variations overtake a given threshold (3° in this work) during a conical

https://doi.org/10.5194/egusphere-2026-4286
Preprint. Discussion started: 31 July 2026

scan. Second, as the CNR decreases, the algorithm produces more and more velocity outliers. Velocity data below a given CNR threshold (-22 dB in this work) are thus also replaced by *nans*. So far, these thresholds have been determined empirically by observing the wind data, but automatic thresholding methods could be implemented in future works.

The second step for wind computation is the lidar own-speed subtraction. Indeed, as stated before, the velocity profiles resulting from the first step characterize the airflow speed with respect to the (moving) lidar. The lidar own speed vector with respect to the ground, i.e. the aircraft groundspeed, must therefore be subtracted. This operation requires great care, considering that it is typically 10 to 100 times higher than typical PBL wind speeds. Errors in subtracting the lidar groundspeed can thus strongly impact wind vectors retrievals. As introduced before and schemed on Figure 2, this subtraction can be done following two techniques.

The Lidar Ground-Echo (LGE) technique uses the ground laser echo to measure the Doppler shift created by the lidar speed relative to the surface. Using surface echoes recorded during a conical scan, the groundspeed vector is estimated using the same algorithm as for the atmospheric backscatter signal. Since the cone-averaged CNR is usually high for ground echoes, a standard VAD-based fitting algorithm can be used. Then subtracting the groundspeed vector from the air velocity vector directly provides the wind vector. Nevertheless, the latter is obtained in the lidar framework. Two successive framework rotation matrices must therefore be applied to obtain the wind vector in the conventional Earth frame. The first one is a lidar-to-aircraft rotation matrix, that corrects for smalls misalignment between the lidar frame and the aircraft frame. As discussed in Sect.2.3, this matrix can be estimated using a calibration procedure. The second is the aircraft-to-Earth rotation matrix, that corrects for the attitude angle changes (roll, pitch and yaw) of the aircraft during the flight, with respect to the Earth frame. This matrix is known as the Euler transformation matrix, and its expression can be found in aerodynamics textbooks (Stengel, 2005) or in previous airborne lidar works (Kavaya et al., 2014 or Zhang et al., 2024 for instance). It is updated dynamically for each conical scan, using the roll, pitch and yaw data provided by the aircraft inertial navigation sensors. In the ATR-42, these data come at a rate of 10 Hz, much faster that the conical scan duration (17 s), such that the data rate is not a limitation. After these two rotations (lidar-to-aircraft, then aircraft-to-Earth), LGE-based wind profiles are obtained in the Earth frame.

The second technique for aircraft groundspeed subtraction relies on the aircraft Flight Test Instrumentation (FTI), namely the GPS sensor, which provides directly aircraft groundspeed vectors in the Earth frame of reference. As schemed on Figure 2, the two rotation matrices (lidar-to aircraft, then aircraft-to-Earth) must therefore be applied to air velocity vectors, before subtracting the FTI-derived groundspeed. After subtraction, the desired FTI-based wind product is obtained.

The FTI-technique is very attractive because it can be used regardless of ground visibility conditions. It also appears simpler since there is no need to estimate the aircraft groundspeed from the lidar data. The main issue is that the rotation matrices have to be applied to air velocity vectors (air speed with respect to the aircraft), which are high-magnitude vectors, generally more than 100 $m.s^{-1}$. This magnitude amplifies any inaccuracy of the rotation transformations, which puts stringent constrains on

https://doi.org/10.5194/egusphere-2026-4286
Preprint. Discussion started: 31 July 2026

the quality of their estimation (discussed in Sect. 2.3 and Sect. 3.4). On the contrary, with the LGE technique, the aircraft groundspeed is measured within the same frame as the air velocity. Therefore, it is subtracted from the air velocity *before* applying the rotation matrices. The latter then applies to vectors with much lower magnitudes, and the resulting wind profiles are thus less sensitive to imperfections in the knowledge of rotation angles. Nevertheless, as already mentioned, a major limitation of the LGE-technique is that it cannot be applied when clouds hide the ground, a situation likely to be encountered in many places. Over water surfaces, it can also be biased by the waves motion, while FTI groundspeed data cannot.

Eventually, LGE-based and FTI-based wind profiles computed with the former steps are obtained on a vertical axis relative to the aircraft flight altitude, which is time-varying during the flight. They are also distributed slightly unevenly in time, depending of the exact clock-time of each conical scan. Consequently, in a final processing step (not represented in Figure 2), all the wind profiles are linearly interpolated on an evenly spaced grid in time (21 s time-steps) and altitude (30 m altitude steps, hence resulting in a total oversampling factor of 5 with respect to the vertical resolution of 150 m).
Table 1 summarizes the properties of wind and CNR vertical profiles provided by LIVE during the MAGIC-2021 campaign. For this campaign, only profiles of the horizontal wind vector (u and v components) are made available. The data can be downloaded from AERIS website (see *Data Availability* section). In fact, profiles of the vertical wind component w are also computed, but since this component is very weak, it is more sensitive to bias. Quality checks and dedicated analysis for the vertical wind w remain to be carried out in future works.

Table 1. Main properties of wind profiles measured by the airborne CDL Lidar LIVE

Parameter	Value	Comment
Horizontal resolution	Across-track: 2.5 km Along-track: 1.8 km	At 5000 m ground-relative flight altitude, 100 m.s^{-1} aircraft groundspeed, 17 seconds cone duration, 21 seconds full-scan period
Horizontal sampling rate	2.1 km	
Vertical resolution	150 m	Determined by the laser pulse duration of 1 µs
Vertical sampling rate	30 m	Oversampling by a factor of 5 w.r.t. vertical resolution
Vertical blind zones	300 m below aircraft and above strongly-scattering objects (ground, sea…)	Determined by the pulse duration and tails shape
Lidar ambiguity range	10.7 km	Determined by the laser PRF. Maximum flight altitude was 8 km

2.3 Computation and calibration of the lidar-to-aircraft rotation matrix

It is essential to estimate correctly the lidar-to-aircraft rotation matrix mentioned in Sect.2.2. This can be done using a flight, or a portion of flight, performed under clear weather conditions, such that the ground echoes can be measured by the lidar. This enables recording simultaneously groundspeed vectors in the lidar frame, following the LGE method, and groundspeed vectors in the Earth-frame, given by the FTI. Applying the inverse Euler transformation matrix to FTI-based groundspeed vectors converts them into the aircraft frame, where they can be compared to the LGE-derived groundspeed vectors.

https://doi.org/10.5194/egusphere-2026-4286
Preprint. Discussion started: 31 July 2026

For the MAGIC-2021 campaign, only two flights turned to be appropriate to perform this task: the preliminary flight in France (11/08/2021), and the very last flight of the campaign (26/08/2021). The four other flights were characterized by frequent clouds and did not offer proper ground visibility. Obviously, we have used the preliminary flight, so that the derived lidar-to-aircraft rotation matrix could be used for the following flights. Figure 3a shows the components of FTI groundspeed vectors expressed in the aircraft frame, against the LGE groundspeed vectors, before applying any corrective lidar-to-aircraft rotation matrix. A clear misalignment can be seen along the y and z directions (respectively, pitch and yaw rotation axes). A maximum likelihood estimator, detailed in Appendix A, is then employed to compute the corrective lidar-to-aircraft rotation matrix, using only data points recorded over dry land and during steady flight conditions (roll, pitch or yaw excursions below 3°). Because the lidar is mechanically pre-aligned to the aircraft frame, the estimation procedure assumes that rotation angles are small, which enables linearizing the rotation matrix. For the flight of August 11th, rotation angles estimates (see Appendix A) are found to be small indeed: $\theta_x = +0.00 \pm 0.21°$, $\theta_y = -0.93 \pm 0.03°$, $\theta_z = +3.25 \pm 0.05°$. As shown in Figure 3b, rotating the LGE dataset by these angles re-aligns LGE and FTI data.

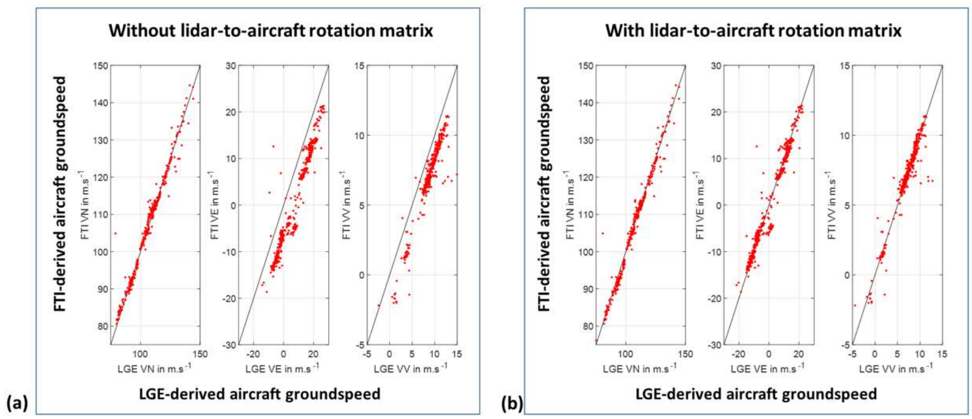

Figure 3. FTI-derived groundspeed in the aircraft frame, against the LGE-derived groundspeed, before (left) and after (right) applying the corrective lidar-to-aircraft rotation matrix. Measurements are shown as red dots. Black lines have a zero-intercept and a slope of one.

Though these corrective angles are small, they are essential for retrieving winds correctly. As also shown in Appendix A (Eqs. (A.17) and (A.19)), neglecting to apply the lidar-to-aircraft rotation could lead to a wind measurement bias approximated by:

$$b_{max}=V_x\left(\theta_y^2+\theta_z^2\right)^{1/2} \qquad (1)$$

Where V_x is the x-component, in the aircraft frame, of the vector to which the rotation matrix is applied. As mentioned in Sect.2.2, for the FTI-based wind product, the rotation matrix is applied to air velocity vectors, which are high-magnitude

https://doi.org/10.5194/egusphere-2026-4286
Preprint. Discussion started: 31 July 2026

vectors. For a typical air velocity V_x=100 m.s^{-1}, this would lead to a catastrophic measurement bias as high as ± 5.9 m.s^{-1} in modulus. If the rotation matrix is applied, a measure of the potential residual bias can be obtained by replacing the true misalignment angles in the preceding formula by the standard deviations of their respective estimates (Eq. (A.18)). In this case, the potential bias reduces to only ± 0.1 m.s^{-1} in modulus, which can be considered negligible in this work compared to other noise sources discussed later on. For the LGE-based wind product, applying the lidar-to-aircraft rotation is less critical because the matrix is applied to wind-vectors, with much lower magnitude. In the PBL, assuming a 5 m.s^{-1} wind along the aircraft x-axis, the bias, if the lidar-to-aircraft rotation is not applied, is limited to 0.3 m.s^{-1}. Nevertheless, winds can be much stronger at high altitude. During the MAGIC-2021 campaign, wind magnitudes up to 35 m.s^{-1} have been recorded. In such case, even for the LGE-based wind product, neglecting to apply the lidar-to-aircraft rotation could lead to significant bias exceeding 2 m.s^{-1}. It is therefore beneficial to apply it even for the LGE-based wind product.

During the MAGIC-2021 campaign, we have used the lidar-to-aircraft rotation matrix derived from the flight of August 11th for all the other flights of the campaign. This decision was forced by weather conditions, since all the following flights encountered cloudy conditions with only partial ground visibility. Yet it was questionable whether this matrix would remain valid until the end of the campaign (August 26th). Fortunately, on this last day, good weather conditions were met again, and the matrix could be re-estimated for comparison. Rotation angles (θ_x = +0.22 ± 0.29°, θ_y = -0.89 ± 0.02°, θ_z = +3.30 ± 0.03°) were found to be very close from those derived on August, 11th. The angle difference is below 0.05° for the y and z components, which translates into a negligible wind difference below 0.1 m.s^{-1} for V_x=100 m.s^{-1}. The angle difference is bigger for the x-axis rotation (0.2°), nevertheless Eq.(1) shows that θ_x does not enter at first order into the equation governing the wind bias.

It is important to note that applying the lidar-to-aircraft rotation matrix only permit to cancel an average measurement bias. Yet the correction is not perfect for each individual conical scan. In other words, residuals discrepancies remain between FTI and LGE groundspeed vectors, that can be modeled as a zero-mean random noise. This noise will be discussed and characterized later on Sect.3.3.

To summarize this section, it has been shown that estimating and applying the lidar-to-aircraft rotation matrix is required for deriving correctly the FTI-based wind profiles. This ensures long-term measurement bias to remain below 0.1 m.s^{-1}, though some random noise remains (characterized later on). Using this lidar-to-aircraft matrix is also beneficial, though less critical, to derive the LGE-based wind profiles. Finally, using the same matrix for all the flights of the MAGIC-2021 campaign (in this work, the August 11th matrix) has been shown to be a valid choice.

https://doi.org/10.5194/egusphere-2026-4286
Preprint. Discussion started: 31 July 2026

3 – Results

In this section, we first present a brief summary of the MAGIC-2021 campaign for LIVE, before presenting CNR and wind profiles results for two flights realized by clear weather. These flights are used to illustrate the respective advantages and limitations of LGE-based and FTI-based wind profiles, and to compare them quantitatively. Then we show measurement results for a flight with mixed clear and cloudy conditions. The latter, as well as two other flights that are not fully described in this paper, are used to assess the validity of lidar wind measurements, compared to radiosonde wind measurements. Finally, the lidar wind profiles are compared to a completely independent data set, made of simulated wind fields provided by ECMWF.

3.1 Campaign overview for the airborne Doppler Lidar

Six successful flights have been conducted with LIVE during the campaign, totalizing about 21 hours of data and allowing to measure almost 60 000 independent horizontal wind vectors (the data set contains five times more data points, considering the vertical oversampling rate of 5 mentioned in Sect.2). Table 5 summarizes flight locations, durations, potential number of wind data and effectively retrieved wind data. The potential number of wind data is defined as the number of 150 m vertical intervals (lidar resolution) between the aircraft altitude and the ground altitude, integrated along the flight trajectory. A variable fraction (80% in average) of this potential number is available for wind estimation, some data being unavailable because of lidar blindness (below clouds, below the aircraft, above SSO – see Table 1), or because of sporadic acquisition or laser emission issues. As mentioned in Sect.2.2, two filters are applied to available wind measurements, that suppress expected bad data and outliers: an attitude angle filter suppresses all the conical scans recorded during unsteady flight attitude conditions (over 3° deviations in roll, pitch and yaw), and a CNR filter suppresses all data points below a threshold CNR of -22 dB. In the end, summing over the six different flights, the number of valid data for analysis is about 50% out of the total potential data number. Ways for improving this fraction in future works are discussed along the paper and summarized in the paper conclusions.

Table 2. Summary of flights conducted with the airborne Doppler Lidar LIVE during the MAGIC-2021 campaign, including the test flight in France. The star-signs (*) indicate flight results detailed in this paper.

Flight date (2021)	Location	Flight duration	Number of independent wind data			
			Total Potential	Fraction available before filtering	Fraction valid after 1st filter (attitude angle threshold)	Fraction valid after 2nd filter (CNR threshold)
11/08 (*)	France	3h13	23 155	88.1%	70.6%	52.1%
17/08	Sweden & Finland	2h36	12 891	63.7%	41.3%	38.4%
23/08 (*)	Sweden	4h18	20 897	77.9%	48.5%	45.1%
23/08	Sweden	2h43	16 461	68.5%	43.0%	36.6%
26/08	Sweden	3h19	17 988	83.9%	54.1%	50.6%

https://doi.org/10.5194/egusphere-2026-4286
Preprint. Discussion started: 31 July 2026

26/08 (*)	Sweden & Norway	4h39	28 115	88.5%	68.1%	61.8%
	Total	20h48	119 507	96 102 – (80.4%)	67 772 – (56.7%)	58 925 – (49.3%)

3.2 Clear weather flight n°1 (preliminary flight in France, 11/08/2021)

Prior to science flights in the Arctic, a test flight at altitude 7-8 km took place in South-West France, from Francazal airport (near Toulouse), which hosts SAFIRE's facility. The flight pattern is shown in Figure 4. It enabled flying over South-West plains, the Atlantic Ocean, and Pyrenees mountains. This flight is the one used for calibrating the lidar-to-aircraft rotation matrix, as previously discussed in Sect.2.3.

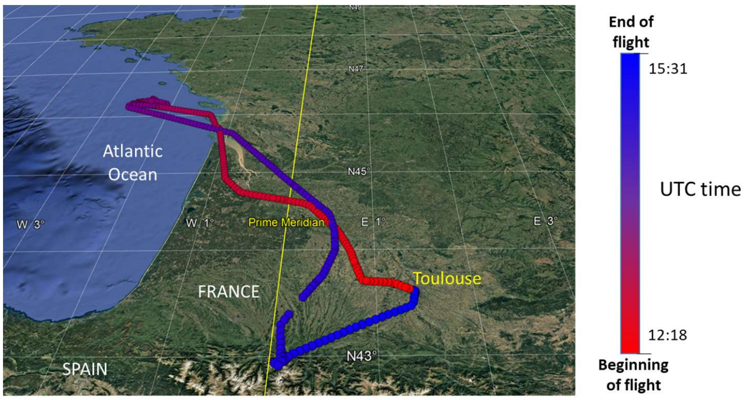

Figure 4. Test flight in France (11/08/2021). The aircraft trajectory is shown in color gradient. Map data © Google; contains modified Landsat data © USGS/NASA; contains modified Copernicus Sentinel data © ESA & European Commission; additional data © SIO, NOAA, U.S. Navy, NGA; bathymetry © GEBCO Compilation Group.

https://doi.org/10.5194/egusphere-2026-4286
Preprint. Discussion started: 31 July 2026

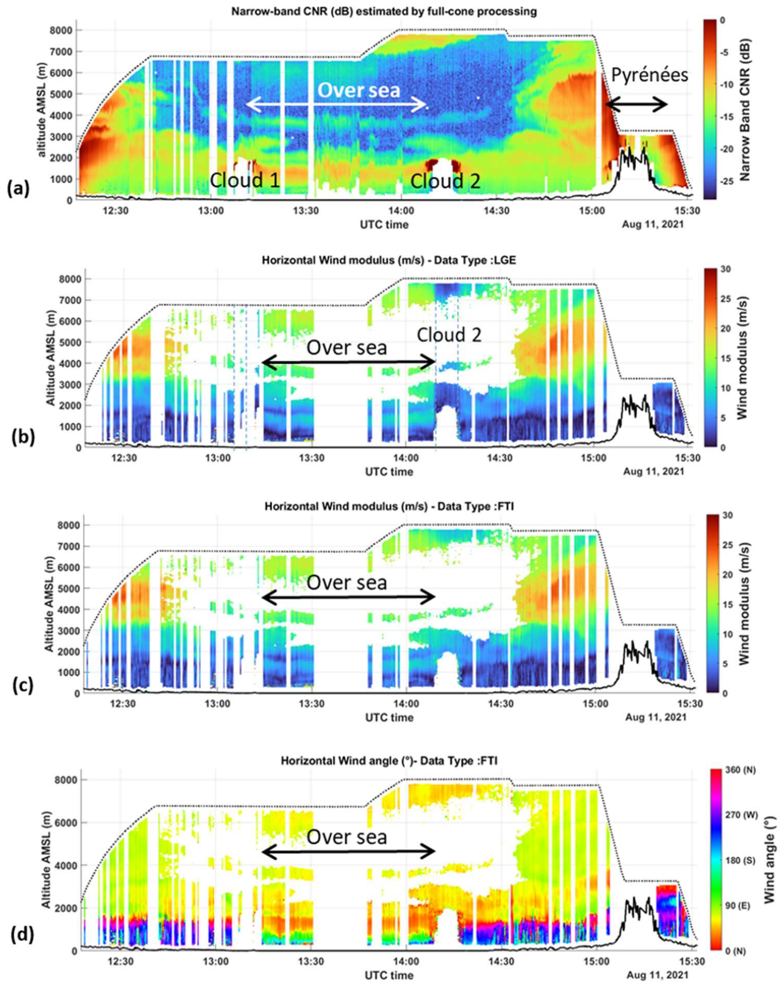

Figure 5. Test flight in France (11/08/2021) – Lidar measurements as functions of time (UTC) and altitude. a) Lidar CNR in dB; b) LGE-based wind modulus in m.s^{-1}; c) FTI-based wind modulus in m.s^{-1}; d) FTI-based wind angle in degrees, clockwise from north (0°N, 90°E, 180°S, 270°W). Black lines (bottom solid, top dashed) indicate ground and flight altitudes above mean sea level (AMSL).

Figure 5a displays a curtain plot of measured scan-averaged CNR vertical profiles during this flight. Since the CNR is proportional to the aerosol backscattering coefficient, it provides information on the aerosol layer structure. Range-correcting

https://doi.org/10.5194/egusphere-2026-4286
Preprint. Discussion started: 31 July 2026

the CNR (i.e. multiplying it by the squared range z^2) would give a better picture of the aerosol layers, but in this paper, we chose to stick to the CNR representation. Indeed, as mentioned in Sect.2, CNR profiles are also used for thresholding data and filter wind outliers. Vertical white stripes on the CNR plot correspond to missing data (when the acquisition or the laser is off). Lidar blind zones are also shown in white (300 m below the aircraft, 300 m above SSO, and all the way below optically-thick clouds). The bottom, solid black line represents the above-mean-sea-level (AMSL) ground altitude, according to SRTM30 Digital Elevation Model (DEM), while the top, dashed black line shows the aircraft flight altitude as given by FTI sensors. Both altitudes refer to the EGM96 geoid. CNR data indicate strong aerosol scattering conditions over the plains, especially near Toulouse, where the vertical extension of the aerosol layer is seen to be very large (up to 6 km). Oversea, a maritime aerosol layer is observed at 1-1.5 km, while the atmosphere is much more pristine at higher altitudes. The disturbed and upshifted CNR patterns occurring between 13:30 and 13:45 and at 14:00 below 2000 m are due to bending manoeuvres performed by the ATR crew at these times. A high-altitude aerosol layer (7-8 km) is captured below the aircraft at its highest flight level. Only two optically thick clouds are met, around 13:10 and 14:15, during the two crossings of the Atlantic shore.

Figure 5b/c/d display wind products (discussed hereafter). Compared to CNR plots, they all show additional white areas (*nan* data). As stated before, they result from the two filters that suppress data when the aircraft pitch, roll, or yaw angles variations exceed 3° during a conical scan (which occurred frequently during this flight, especially during bending and spiraling manoeuvres), and when the CNR is below the required threshold (-22 dB in this work). In future works, this CNR-threshold outlier-filtering technique could probably be improved, using moving median filters for instance. Time-averaging or spatial averaging low-CNR columns could also permit to lower the threshold and recover more wind data, at the expense of resolution, as previously demonstrated for instance in Witschas et al. (2020). Despite the current limitations, it can be highlighted that between 14h30 and 15h, the lidar delivers wind measurement all the way from the aircraft to the ground, demonstrating 7.5 km of full-range performance without averaging. This is close to the world's best range performance reported in Yew et al., 2025 for vertical profiling from an airborne platform.

Figure 5b and 5c respectively display the LGE-based and FTI-based horizontal wind magnitude profiles. The main noticeable difference between them is seen above the second cloud, where the LGE-based wind values appear strongly biased and close to zero, whereas the FTI-based values show physical continuity before and after the cloud. This is because the LGE technique, as currently implemented, computes the aircraft groundspeed using the last measurable lidar echo. When optically-thick clouds hide the ground, the last echo comes from the cloud top. Therefore, the lidar speed relative to the cloud, instead of the ground, is subtracted from the velocity-profile, and the result is an apparent wind close to zero. In such situation, the FTI-technique is more appropriate, as expected. A closer look would also reveal slight differences in the LGE and FTI-based wind values over sea, the former being biased because of the waves motion, but this will be evidenced more clearly in Sect.3.4. Finally, one can notice that FTI-based profiles show a slight vertically grooved pattern, whereas LGE profiles do not. Vertical grooves suggest

https://doi.org/10.5194/egusphere-2026-4286
Preprint. Discussion started: 31 July 2026

that this noise originates from inaccuracies when subtracting the aircraft groundspeed. Indeed, since the same groundspeed is subtracted to all the velocity values of a vertical profile, any error on the groundspeed expands vertically on the wind profile column. Using bold characters for vectors, we shall write this excess noise by the relationship $\boldsymbol{W_{FTI}} = \boldsymbol{W_{LGE}} + \boldsymbol{n}$, where $\boldsymbol{W_{FTI}}$ and $\boldsymbol{W_{LGE}}$ designate the FTI and LGE horizontal wind vectors at a given position in time and altitude, and $\boldsymbol{n}$ the excess noise vector. Also in Sect.3.4, this noise vector will be characterized, and its origin discussed.

Figure 5d shows the FTI-based horizontal wind pointing direction. The chosen angle convention is clockwise from north (0°N, 90°E, 180°S, 270°W). The vertical evolution of wind direction is seen to be spatially homogeneous throughout the flight, pointing NE in altitude and SW in the lower troposphere, except oversea where a SE-oriented layer is clearly seen below 1000 m. Over the continent, the 180° wind rotation layer (in red) is seen to be located between 1 and 2 km, elevating with the ground level up to 3 km over the mountains.

3.3 Clear weather Flight n°2 (last flight in Norwegian sea, 26/08/2021)

The last flight of the campaign took place on August 26th in the afternoon. As shown in the flight map Figure 6, the goal was to reach the Norwegian sea and fly short legs downwind over several oil and gas offshore platforms. Good weather conditions were met, and all the flight was conducted at constant flight altitude (5.7 km). The lidar data outcome is excellent on this flight, with more than 17 000 independent wind measurements available after filtering. However, numerous short legs were performed in the platform area, implying a large number of steep bends. This pattern limited the wind profile retrieval rate in this area. Only FTI-based wind profiles are displayed here for this flight, but the difference between LGE and FTI profiles is discussed in Sect.3.4.

https://doi.org/10.5194/egusphere-2026-4286
Preprint. Discussion started: 31 July 2026

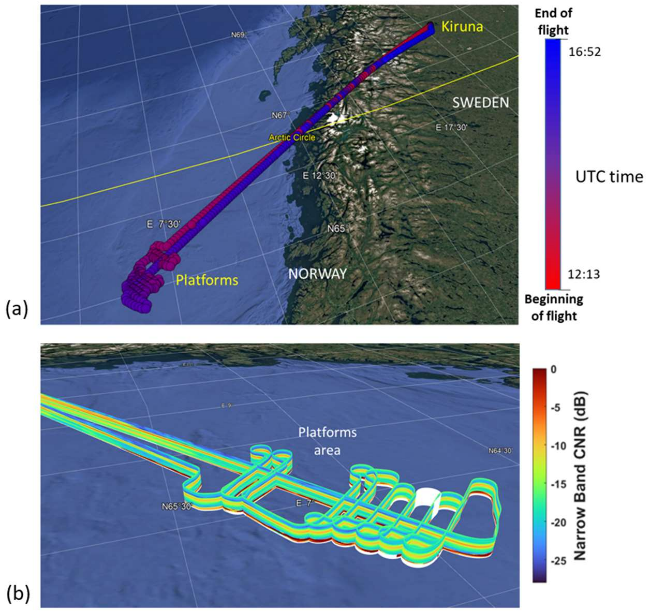

Figure 6. Science flight in Norway (26/08/2021). (a) Aircraft trajectory shown in color gradient; (b) Details of the flight trajectory near the platforms. Here the lidar CNR is shown in 3D. Map data © Google; contains modified Landsat data © USGS/NASA; contains modified Copernicus Sentinel data © ESA & European Commission; additional data © SIO, NOAA, U.S. Navy, NGA; bathymetry © GEBCO Compilation Group.

https://doi.org/10.5194/egusphere-2026-4286
Preprint. Discussion started: 31 July 2026

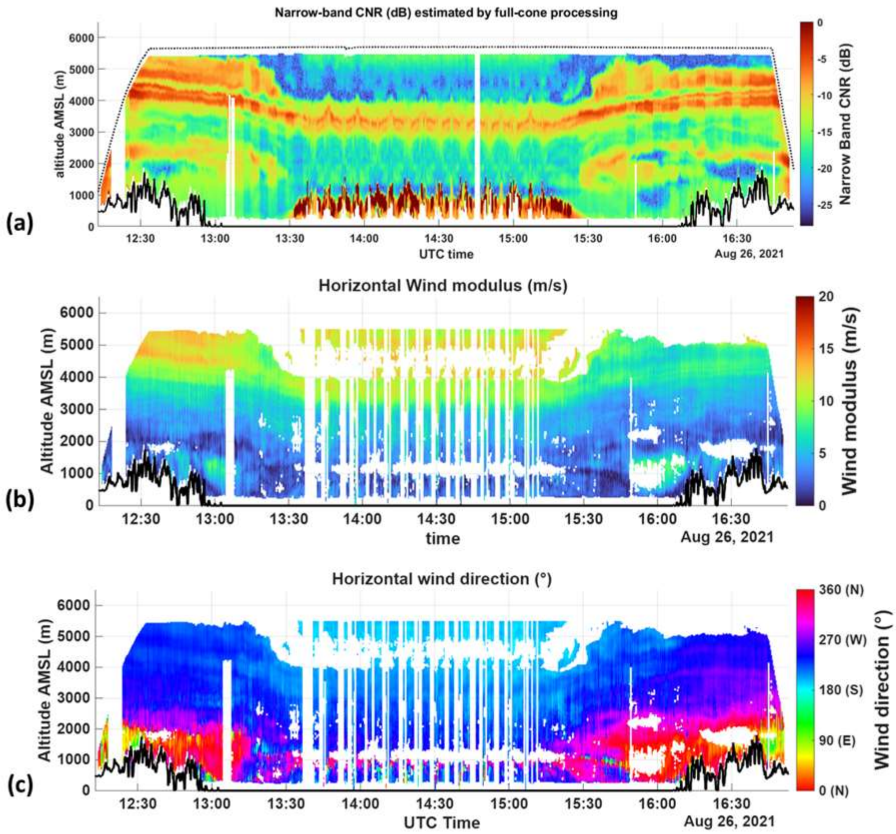

Figure 7. Science flight in Norway (26/08/2021) – Lidar measurements as functions of time (UTC) and altitude. a) Lidar CNR in dB; b) FTI-based wind modulus in m.s^{-1}; c) FTI-based wind angle in degrees, clockwise from north (0°N, 90°E, 180°S, 270°W).

Figure 7a shows the recorded CNR profiles. Some vertical intensity-modulated bands can be seen, corresponding to laser power variation tests. Aerosol layers evolution at the ground/sea interface can be seen with fine details. In the platform area, a low altitude maritime haze was encountered, which also complicated lidar measurements. Figure 7b and 7c show the recorded FTI-based wind profiles in modulus and direction respectively. The numerous vertical white stripes at the figure center result from the numerous bends (roll angle variations >3°) made by the aircraft in the platform area. Wind vertical gradients in modulus are quite homogenous spatially all along the flight, but a clear vertical shift of the probed airmass is seen (lower over sea than over ground). Close to the shore, a low altitude air parcel with higher speed is also clearly detected around 13:00 and

https://doi.org/10.5194/egusphere-2026-4286
Preprint. Discussion started: 31 July 2026

16:00. The wind direction over sea is pointing mainly SW, which is consistent with the chosen orientation of flight legs (orthogonal to the wind). Below 3000 m, over ground and at the ground/sea interface, the wind is seen to rotate and point to north direction. Above the mountains, fine details and wind direction variations can also be observed, for instance between the Swedish and Norwegian slopes.

3.4 Quantitative comparison of LGE-based and FTI-base wind profiles

The two flights described above, August 11th and August 26th, are suitable for comparing LGE-based and FTI-based wind products, since ground visibility was very good, except for a few clouds. According to Figure 2, LGE-based and FTI-based profiles both derive from the same air velocity profile, from which two different aircraft groundspeed are subtracted. Consequently, computing the difference between LGE and FTI wind products is mathematically tantamount to computing the difference between LGE and FTI groundspeed vectors, expressed in the Earth frame. Comparing both groundspeeds has already be discussed in Sect.2.3, in order to derive the lidar-to-aircraft rotation matrix, but it was in the aircraft frame. For a direct interpretation in terms of wind measurements, the analysis of residuals is performed here in the Earth frame.

Using bold characters again to designate vectors, let us note $\boldsymbol{\Delta_W} = \boldsymbol{W_{FTI}} - \boldsymbol{W_{LGE}}$ the difference between two wind vectors expressed at the same point of time and altitude. As noted above, for all vectors of the same wind column this difference is equal to the difference of groundspeed vectors $\boldsymbol{\Delta_W} = \boldsymbol{\Delta_{GS}} = \boldsymbol{GS_{FTI}} - \boldsymbol{GS_{LGE}}$ recorded at the same time, and expressed in the Earth frame. Over dry land, the groundspeed difference is expected to be zero up to measurement noise, i.e. $\boldsymbol{\Delta_{GS}} = \boldsymbol{n}$, with $\boldsymbol{n}$ the noise vector introduced previously in Sect.3.2. Over sea, because of the waves motion, we expect to have $\boldsymbol{\Delta_{GS}} = \boldsymbol{n} + \boldsymbol{V_{sea}}$, with $\boldsymbol{Vsea}$ the average 2D (horizontal) sea speed vector.

Figure 8 shows the zonal and meridional components, noted Δu and Δv (scalars), of the groundspeed difference vector $\boldsymbol{\Delta_{GS}}$, for the two flights discussed above. Data points corresponding to ground (dry land) and sea are shown with different colors, delimiting distinct data clouds. The sea speed vector between the cloud's centers can thus be derived. Estimated sea speed magnitudes are in the range of 1.8 and 1.6 m.s^{-1} for both flights, and sea speed orientations are consistent with the wind orientations measured by the lidar in the lowest atmospheric layer above sea level (see Figure 6d and Figure 7c), pointing SE and SW respectively for the flights of August 11th and 26th.

https://doi.org/10.5194/egusphere-2026-4286
Preprint. Discussion started: 31 July 2026

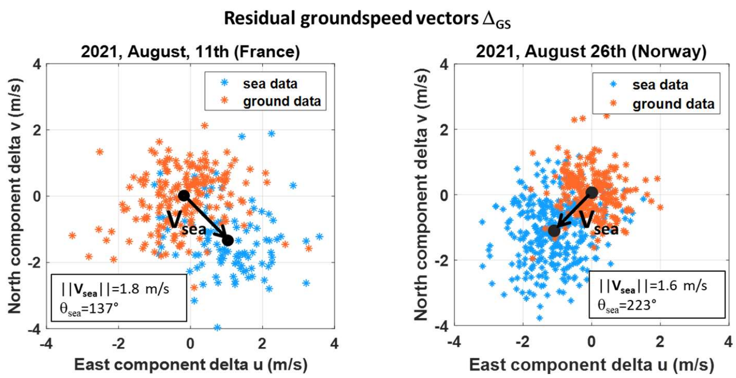

Figure 8. Residual groundspeed vectors Δ_{GS}=GS_{FTI}-GS_{LGE} above ground and sea, for the flights of August 11th and 26th (clear weather flights). Black dots mark the distribution centers of orange and blue data clouds. The vector between the two black dots indicates the average sea speed vector.

Table 3 indicates the statistical mean and standard deviations of the noise vector **n** along the u and v dimensions, using only the data recorded above ground (orange clouds) for the two flights. In each case, the noise vector distribution is very close from being centered and circular (i.e. Δu and Δv both have means close to zero and nearly equal standard deviations). We have also checked that histogram shapes of Δu and Δv are close from gaussians. The distribution standard deviations are about 0.8 $m.s^{-1}$ for August 11th flight, and 0.6 $m.s^{-1}$ for August 26th flight.

Table 3. Statistical properties of the noise vector Δ_{GS}=n recorded above ground for two flights

Flight date	Location	Data points over ground	Statistical properties of the noise vector Δ_{GS}=n			
			Δu ($m.s^{-1}$)		Δv ($m.s^{-1}$)	
			Mean	Std	Mean	Std
11/08/21	France	200	-0.18	0.84	+0.02	0.85
26/08/21	Sweden & Norway	230	0.0	0.57	0.06	0.59

The origin of this excess noise for FTI-based wind profiles is attributed to aircraft vibrations, and slight aircraft deformations that are expected to occur during sudden pitch, roll and yaw changes. Such mechanical distortions probably induce small and random differences between the true physical rotation matrices that should be applied to successive conical scan, and those that are used in practice. Such noise would be expected to be more amplified (thus more visible) in FTI-based profiles than in

https://doi.org/10.5194/egusphere-2026-4286
Preprint. Discussion started: 31 July 2026

LGE-based profiles, because of the difference in magnitude between the vectors to which rotation matrices apply. This would explain why this noise is much more visible on FTI-based profiles, and also the reason why the standard deviation of the noise is higher for August 11th flight. Indeed, numerous bends and spirals were performed during this flight, including above dry land, whereas August 26th flight was mainly a straight flight for the part above ground, implying smoother and more limited aircraft attitude changes. We thus believe that a standard deviation of 0.6 $m.s^{-1}$ for the excess noise vector **n** is representative of the current lidar performances during a straight aircraft trajectory, due to random vibrations only.

To summarize, it has been illustrated that the FTI-based wind product is more generally usable than the LGE-based wind product, being unbiased even in case of cloud cover or sea motion. Yet FTI-based profiles exhibit an excess, column-wise random noise, probably due to inaccuracies of the applied rotation matrices during the flight because of vibrations and sudden attitude angle changes. This noise vector has a gaussian circular distribution along u and v components, with standard deviations in the range of 0.6-0.8 $m.s^{-1}$. This random noise could probably be reduced in future works by locating the aircraft inertial sensor (recording FTI data) closer to the lidar, so that both could share exactly the same framework variations during the flight. During the MAGIC-2021 campaign, the inertial sensor and the lidar were located on opposite sides of the aircraft. Nevertheless, despite this slight excess noise, the FTI method has been the preferred technique to process MAGIC-2021 campaign data, since most of the flights have been performed during at least partially cloudy conditions, with also several sequences over sea. As a consequence, all the wind profiles discussed and displayed in the rest of the paper have been computed using the FTI-method, using the lidar-to-aircraft rotation matrix derived on August 11th.

3.5 Mixed clear-cloudy flight (Sweden, 23/08/2021)

The flight conducted in the early morning of August 23rd provides an example of data obtained under mixed clear-cloudy conditions. As shown in Figure 9, the flight took place south of Kiruna (Sweden), and featured an east-west raster flight pattern, as well as two spirals in the vicinity of Gallivàre. The second spiral location was chosen to match with the expected landing point of a ZPD (Zero Pressure Difference) instrumented balloon that was launched from Esrange station a few hours before. The balloon carried various sensors, including a radiosonde that also recorded the vertical wind profiles. Both will be compared in Sect.3.6.

https://doi.org/10.5194/egusphere-2026-4286
Preprint. Discussion started: 31 July 2026

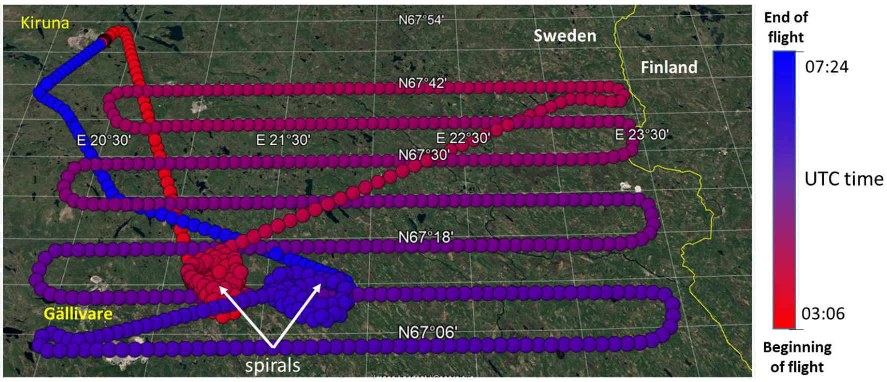

Figure 9. Science flight in Sweden (23/08/2021). Aircraft trajectory shown in color gradient. Map data © Google; contains modified Landsat data © USGS/NASA; contains modified Copernicus Sentinel data © ESA & European Commission.

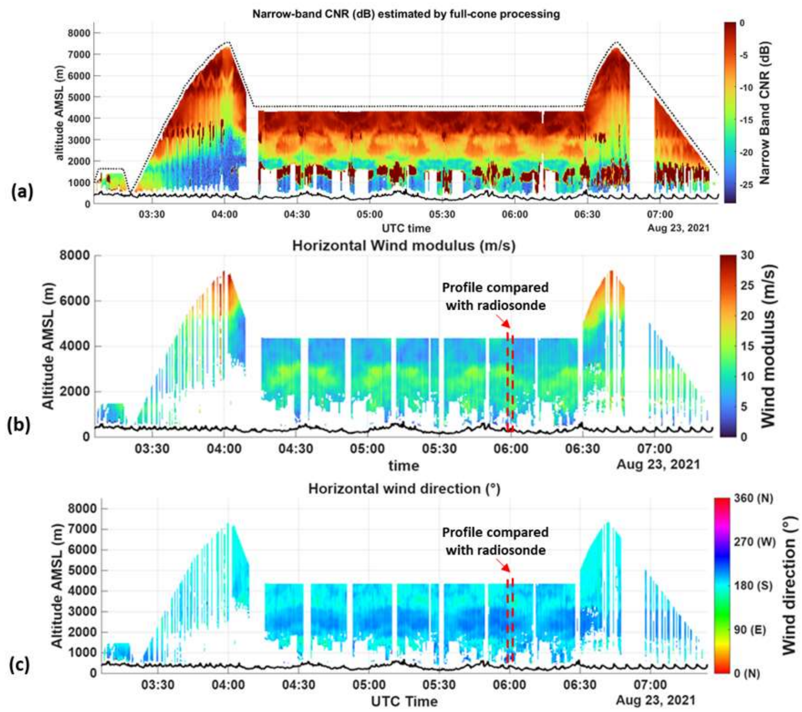

Figure 10. Science flight in Sweden (23/08/2021) – Lidar measurements as functions of time (UTC) and altitude. a) Scan-Averaged lidar CNR in dB; b) Wind modulus in m.s^{-1}; c) Wind angle in degrees, clockwise from north (0°N, 90°E, 180°S, 270°W).

Figure **10** shows recorded CNR profiles during the flight. It can be seen that while the first spiral was performed under almost clear sky conditions, low clouds unfortunately came into the area for the rest of the flight. This situation prevented lidars to conduct successful measurements in the lower layers of the atmosphere. A striking feature is the very strong aerosol backscattering signal recorded in altitude, inducing very high CNR values below the aircraft. This unusual signal is thought to have resulted from the propagation in Scandinavia of airmasses from Canada and Siberia, polluted by massive wildfires in summer 2021 (Jain et al., 2024; Popovicheva et al., 2022). Strong enhancements of carbon monoxide and methane, two gases emitted by fires, were measured at the same time by in situ instruments on-board the ATR-42. Preliminary analysis based on back trajectories simulations conducted by LMD tend to confirm the Canadian and Siberian origins of the sampled air masses. **Erreur ! Source du renvoi introuvable.**b and 9c show the measured FTI-based wind profiles. The profiles are partially unavailable during most of the spirals, because of the attitude angle filter. They are continuously obtained during the raster flight pattern, except at each bend at the leg extremities because of large roll angle variations again. The wind modulus exceeds 20 m.s^{-1} above 5000 m, decreasing quickly with altitude. Data obtained during the constant-level part of the flight (aircraft at 4500 m) indicate that the dynamic of the layers situated between 3000-4000 m and 2000-3000 m are slightly distinct, the former exhibiting a lower wind modulus and a more south-oriented direction. Data below the cloud layers are hardly distinguishable, both because of laser signal attenuation, and relative aerosol depletion below clouds.

3.6 Validation of lidar wind measurements

We now compare lidar wind measurements with other wind data sources, namely radiosonde measurements, ATR-42 Pitot tube measurements, and ECMWF meteorological analyses. Several radiosondes have been used during the campaign (model Meteomodem M20), carried by meteorological balloons. With 1 Hz sampling rate, they provide vertical profiles of wind from the ground up to altitudes exceeding the ATR-42 flight level, thus covering the full vertical range of lidar measurements. Two balloon configurations were deployed: a lightweight balloon, for which wind profiles have been acquired during ascent, and a zero-pressure-difference balloon (ZPD), for which profiles have been acquired during descent (Langot et al., 2025). Three ATR-42 flights were selected to provide comparable wind measurements from both LIVE and radiosondes, two of which are shown in Figure 11. For each case, we selected the lidar profile recorded nearest to the balloon trajectory, referred to as "intercomparison point" on Figure 11. For the flight of August 23rd, already introduced in Sect. 3.4, the radiosonde landed on the indicated red point, under the ATR-42 flight track. On August 26th, the radiosonde crossed the flight track in altitude after the aircraft. Radiosonde data, being subject to high-frequency instrumental noise, are binned and averaged onto the lidar vertical grid, with outliers excluded beyond ±2σ.

https://doi.org/10.5194/egusphere-2026-4286
Preprint. Discussion started: 31 July 2026

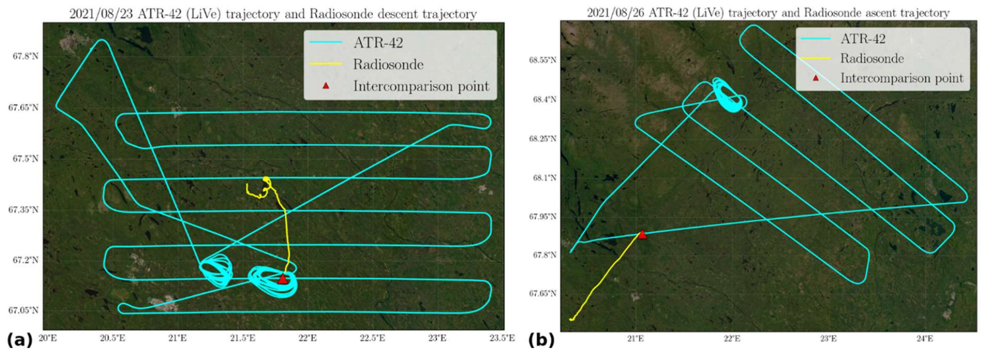

Figure 11. ATR-42 and balloon radiosonde flight tracks on (a) 23/08/2021 and (b) 26/08/2021. Radiosonde vertical wind profiles are compared to LIVE profiles measured at red points. Map data © Google.

Additionally, the ATR-42 was able to perform a wind vertical profile on its own, using its Pitot probe, during the flight of August 23[rd]. The Pitot probe profile was performed during the spiral manoeuvre located above the ZPD-balloon landing site and shortly after the lidar measurement at the same location. Note that the ATR-42 Pitot tube could be thought off as an interesting validation tool for the wind lidar. It offers indeed perfect time collocation with the lidar data, since Pitot tube wind data come at 1 Hz rate, and can be easily interpolated on lidar data times. Unfortunately, because of the lidar blind zone below the aircraft, there is always a minimum of 300 m altitude difference between airmasses probed by the Pitot tube and by the lidar. This difference induces comparison bias, depending of local vertical gradients of wind speed. Therefore, though Pitot tube wind measurements clearly correlate well with lidar measurements below the aircraft, we decided not to use Pitot tube measurements as a quantitative validation tool in this work, except in the case of August 23[rd], where the aircraft spiraling trajectory really allowed to perform a vertical wind profile (though at a slightly different time than the lidar).

Table 4 show acquisition times of the compared wind profiles recorded by radiosondes, lidar and Pitot tube. Time collocation is especially favourable for comparing data from the flights of August 23[rd] and 26[th]. For the flight of August 17[th], the radiosonde wind profile was obtained approximately four hours after the lidar measurement.

Table 4. Acquisition times (UTC) of the wind profiles for the three selected cases.

Flight date	Radiosonde wind profile	LIVE at intercomparison point	ATR-42 wind profile
17/08/2021	12:00–13:21	08:30	–
23/08/2021	02:18–06:01	06:00	06:42–07:38
26/08/2021	06:51–08:05	07:13	–

https://doi.org/10.5194/egusphere-2026-4286
Preprint. Discussion started: 31 July 2026

Wind profiles are also compared to ECMWF ERA5 wind fields, computed using a methodology specified in Schäfler et al. (2010) and Schäfler et al. (2020, Sect. 2c). It uses operational analysis and short-term forecast fields from the Integrated Forecasting System (IFS cycle 41r2) atmospheric high-resolution model (HRES). More precisely, it combines 6-h analysis fields (0000, 0600, 1200, and 1800 UTC) and hourly forecasts initialized from 0000 to 1200 UTC. ERA5 wind fields are then linearly interpolated in time, longitude, latitude, to the lidar data grid. In this section, the lidar vertical altitude grid is converted to a pressure grid, using pressure measurements from the radiosonde interpolated onto the lidar vertical levels, and the lidar wind data are interpolated onto the ERA5 dataset pressure vertical grid.

Figure 12 shows the resulting wind profiles for all three comparison cases. Both the raw radiosonde data and their binned averages are displayed. The comparison is performed for the zonal and meridional wind components (u and v), as well as for the horizontal wind speed $WS=(u^2+v^2)^{1/2}$. Profiles from August 17th (a–c on Figure 12) show good agreement between the lidar and ERA5 profiles. The radiosonde measurements are also in close agreement, but differ slightly, particularly in the meridional wind component, resulting in a horizontal wind speed approximately 2 $m.s^{-1}$ higher. This discrepancy may be attributed to the 4-hour time gap between lidar and radiosonde measurements on that day. August 23rd and 26th flights (d–i on Figure 12), for which measurements had a better time collocation, show clear agreement between radiosonde and lidar wind profiles, throughout the full vertical range. Minor differences appear only below 700 hPa (≈ above 3 km), near the lidar flight level. ERA5 also agrees well with the profiles, although it provides an averaged representation that does not capture the wind speed peaks observed by both the lidar and the radiosonde. The ATR-42 Pitot-tube wind profile from August 23rd is also consistent with the other profiles, but shows slight discrepancies near the surface (above 900 hPa, approximately below 1 km). This could be attributed to higher wind variability at low altitudes, as the aircraft reached these levels nearly one hour after the lidar measurement.

https://doi.org/10.5194/egusphere-2026-4286
Preprint. Discussion started: 31 July 2026

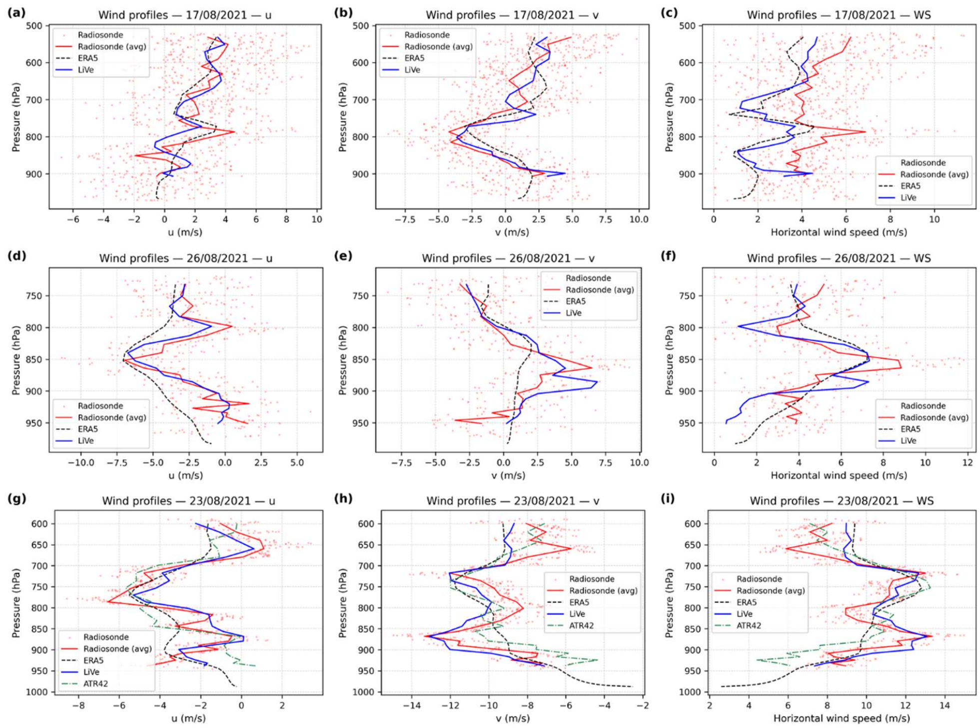

Figure 12. Co-located wind profiles measured by the lidar, radiosonde, ATR-42 Pitot probe and ERA5. Each row corresponds to a different flight: 17/08/2021 (a–c), 26/08/2021 (d–f), 23/08/2021 (g–i). Each column shows a different wind variable: u component (a,d,g), v component (b,e,h), and horizontal wind speed (c,f,i)

In order to quantitatively assess the agreement between lidar and radiosonde measurements, the difference between their wind profiles is computed (Figure 13). We restrict the analysis to the vertical range over which measurements are available for all three cases (725–925 hPa). Wind differences are averaged over the three cases. It can be seen that the difference between lidar and radiosonde measurements does not exceed ±2 m.s^{-1}, and falls below 1 m.s^{-1} for most of the vertical range. This discrepancy is further reduced when excluding the least favorable of the three profiles (August 17th). The mean difference between LIVE and radiosonde measurements is close to zero for both wind components, and remains below 1.5 m.s^{-1} in absolute value throughout the profile. The vertically averaged standard deviation is between 0.9 m.s^{-1} and 1.2 m.s^{-1}. The bias and vertically averaged standard deviations are further reduced when the least favorable of the three profiles (August 17th) is excluded Overall, LIVE wind profiles show good agreement with radiosonde in situ measurements.

https://doi.org/10.5194/egusphere-2026-4286
Preprint. Discussion started: 31 July 2026

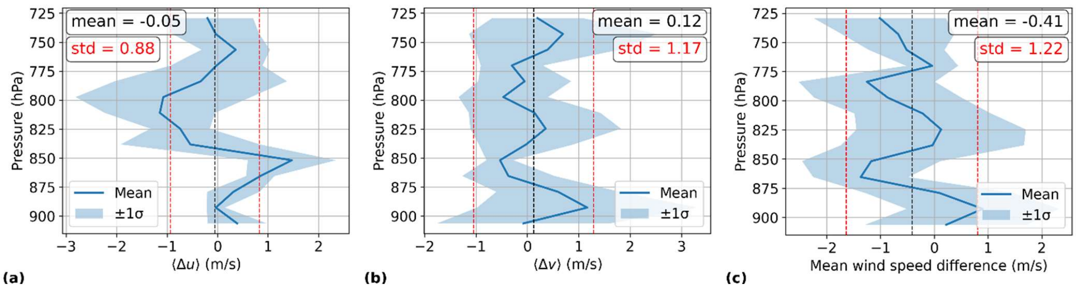

Figure 13. (a–c) Mean wind difference profiles (u,v, and WS residuals) between lidar and radiosonde wind profiles, averaged over the selected comparison cases.

3.7 Extended comparison between LIVE and ECMWF wind profiles

As reported in Sect.3.6, in situ reference sensors are ideal to validate lidar measurements, but the number of available comparison cases during the MAGIC-2021 campaign is very limited, due to the required time and space colocation constraints. On the other hand, ECMWF wind fields can be obtained and interpolated in time and space along the entire lidar grid for each flight. This makes them very attractive for comparison with lidar data. We thus extend in this last section the ECMWF comparison approach to the entire lidar grid. The wind fields are computed from ERA5 using the same methodology as the one mentioned in Sect.3.6. The only difference is that in this section, we found it more practical to interpolate ECMWF wind data to the lidar grid, rather than averaging the lidar profiles to the ECMWF grid, since in the latter case, a single outlier in the lidar data could corrupt the averaging process and spoil neighboring good data.

https://doi.org/10.5194/egusphere-2026-4286
Preprint. Discussion started: 31 July 2026

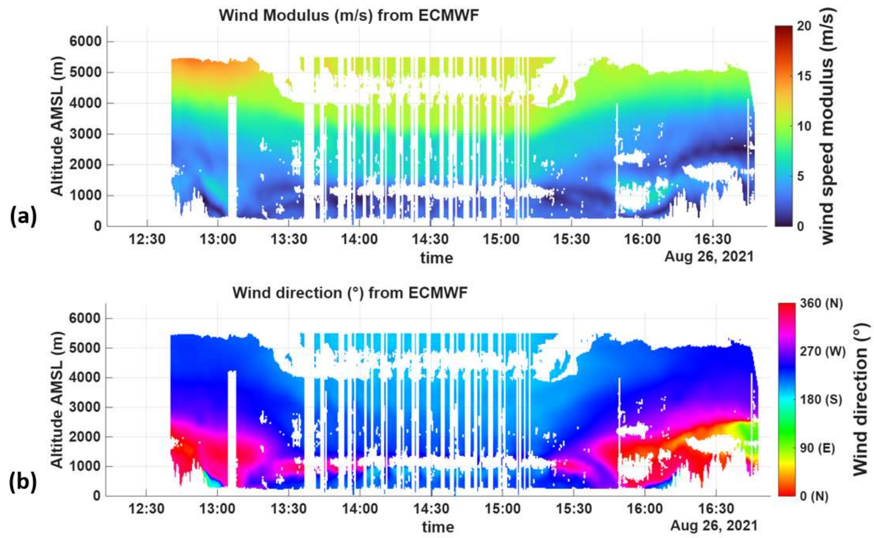

Figure 14. Science flight in Norway (26/08/2021). ECMWF wind fields as functions of time (UTC) and altitude. a) wind modulus in m.s^{-1} b) wind direction in degrees. They can be compared to the lidar results shown in Fig.7b and 7c.

Figure 14 displays ECMWF wind modulus and direction for the flight of August 26th (Norwegian sea flight), that can be compared to the lidar data presented in Figure 7. It is important to note that the lidar data are not assimilated by the ECMWF model. The two datasets are thus completely independent. For better visual comparison, the missing values in the lidar profiles have been reported on ECMWF interpolated profiles. The general agreement between lidar and ECMWF profiles appears visually excellent, with only slight differences noticeable. It can be seen that the lidar as a finer resolution, and captures smaller wind structures than ECMWF data. Like in Figure 8, the difference between lidar and ECMWF wind vectors can be postulated as being a random vector $\boldsymbol{m} = \boldsymbol{W}_{FTI}\text{-}\boldsymbol{W}_{ECMWF}$, resulting from random errors of both lidar measurements and ECMWF modelling process. To verify this, Figure 15a shows the histograms of the zonal and meridional components (Δu and Δv) of $\boldsymbol{m}$, as well as the histogram of it norm $\delta=||\boldsymbol{m}||$. The norm corresponds to the Euclidean distance between lidar and ECMWF vector fields. It is observed that Δu and Δv are almost centered gaussian variables, with similar standard deviations ($\sigma_{\Delta u} \approx \sigma_{\Delta v} \approx 1.4$ m.s^{-1}). In such situation, if Δu and Δv are statistically independent, the norm δ should be approximately Rayleigh-distributed with a probability density given by $f(\delta)=(\delta/\sigma_G^2)*\exp(-\delta^2/(2\sigma_G^2))$, where $\sigma_G \approx 1/2(\sigma_{\Delta u} + \sigma_{\Delta v})$. This is correctly observed on the histogram of δ. The mean of the Rayleigh distribution is μ_δ=1.8 m.s^{-1}, and according to the histogram, 64% of the data show Euclidean distances below 2 m.s^{-1}, and 90% below 3 m.s^{-1}. These values confirm the excellent agreement between lidar and ECMWF wind fields for this flight. Figure 15b shows the point-to-point Euclidean distance δ between lidar and ECMWF

https://doi.org/10.5194/egusphere-2026-4286
Preprint. Discussion started: 31 July 2026

vector fields. It shows that δ is not a spatially white noise, but rather features inhomogeneous spatial correlations, the interpretation of which being beyond the scope of this paper.

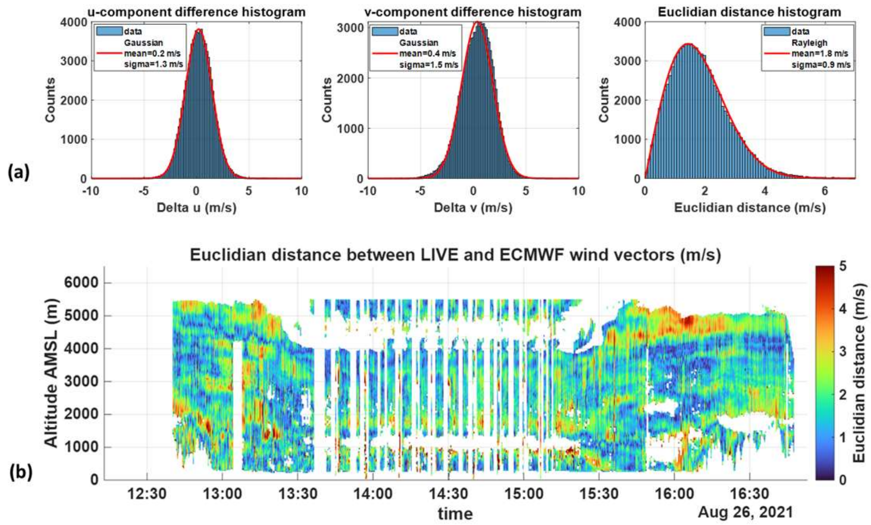

Figure 15. a) Histograms of wind speed differences (zonal component Δu, meridional component Δv, Euclidean distance δ) between the lidar and ECMWF models for the Norwegian sea flight (2021/08/26); b) Point-to-point Euclidean distance δ (in m.s^{-1}) between lidar and ECMWF wind fields

Generalizing the analysis to all the flights of the MAGIC-2021 campaign, Table 5 shows the mean and standard deviations for the zonal and meridional differential wind components (Δu, Δv), as well as the mean Euclidean distance between the lidar and ECMWF wind vectors. Each time, Δu and Δv are found to be almost centered gaussian variables, with close standard deviations. Over six flights, the standard deviations of Δu and Δv always remain within a tight interval, ranging between 1.3 and 2.0 m.s^{-1}.

Table 5. Statistical analysis of the differences between lidar wind field measurements and ECMWF wind field model for all the flights of the campaign. The star-signs (*) indicate flight results detailed in this paper.

Flight date	Location	(W_{FTI}-W_{ECMWF}) m vector statistics between wind fields measured by the lidar and provided by ECMWF re-analysis				
		$\mu_{\Delta u}$ (m.s^{-1})	$\mu_{\Delta v}$ (m.s^{-1})	$\sigma_{\Delta u}$ (m.s^{-1})	$\sigma_{\Delta v}$ (m.s^{-1})	μ_{δ} (m.s^{-1})

https://doi.org/10.5194/egusphere-2026-4286
Preprint. Discussion started: 31 July 2026

11/08/2021 (*)	France	0.3	0.7	1.9	1.6	2.3
17/08/2021	Sweden & Finland	0.3	0.2	1.3	1.5	1.7
23/08/2021 (*)	Sweden	0.4	0.5	1.5	1.9	2.2
23/08/2021	Sweden	-0.8	-0.3	1.5	2.0	2.2
26/08/2021	Sweden	-0.2	-0.4	1.4	1.6	1.9
26/08/2021 (*)	Sweden & Norway	0.2	0.4	1.3	1.5	1.8

In Figure 16 are finally shown the 2D histograms of lidar wind data against ECMWF wind data (wind modulus only), for the six flights reported in Table 5. For an easier visualization, 2D histogram data points with populations below 5 have been discarded. In Figure 16a (test flight in France), the lidar measures slightly stronger winds than given by ECMWF for the lowest and highest modulus values. In the medium-range values, the matrix has a diagonal behavior, yet with some broadening due to the distribution of Δu and Δv between both data sets. The flight of 17/08 (Figure 16b) shows a similar behavior, with a relatively narrow wind speed range during this flight. The first flight of 23/08 (Figure 16c), presented in details in Sect.3.5, shows an even narrower speed range. This is because a limited atmospheric depth was probed during most of the flight, between the low-altitude flight level (4500 m) and the cloud layer (1500-2000 m). Yet the 2D histogram indicates that ECMWF overestimates the brightest magnitude spot by about 2-3 m.s^{-1} with respect to the lidar. The second flight on the same day (Figure 16d) featured a flight sequence at much higher level (8000 m) where the wind magnitude reached up to 35 m.s^{-1}. A clear agreement between ECMWF and the lidar is seen throughout the whole magnitude range, with the exception of lowest speeds, where dispersion increases. Since no wind data could be recorded below 1000 m, the 2D histogram contains no sample with wind magnitude lower than 5 m.s^{-1}. The first flight of 26/08 (Figure 16e) is the only one that exhibits a slight slope discrepancy between the lidar and ECMWF data sets. Throughout almost the whole wind magnitude range, the lidar measures higher modulus by typically +25%. Finally, on the last flight, formerly detailed in Figure 7 and Figure 14, no obvious pattern appears on the 2D histogram (Figure 16f), which exhibits on average a diagonal shape, with slight distortions. Those figures evidence a very good degree of agreement between the lidar data and ECMWF wind fields over the whole campaign. When discrepancies are seen, the analysis cannot tell objectively which of the lidar or the modelled data are closer from the ground truth. Yet it seems more plausible to us that lidar data are closer, for it has been shown in former sections that the lidar captures smaller wind structures than the model. That leads to the suggestion that airborne lidar data would probably be useful to assimilate, whenever available, in ECMWF analysis models and forecasts. More generally, airborne lidar measurements with LIVE may represent a useful validation tool for atmospheric dynamics models, especially in regions of the world with scarce wind measurement stations.

https://doi.org/10.5194/egusphere-2026-4286
Preprint. Discussion started: 31 July 2026

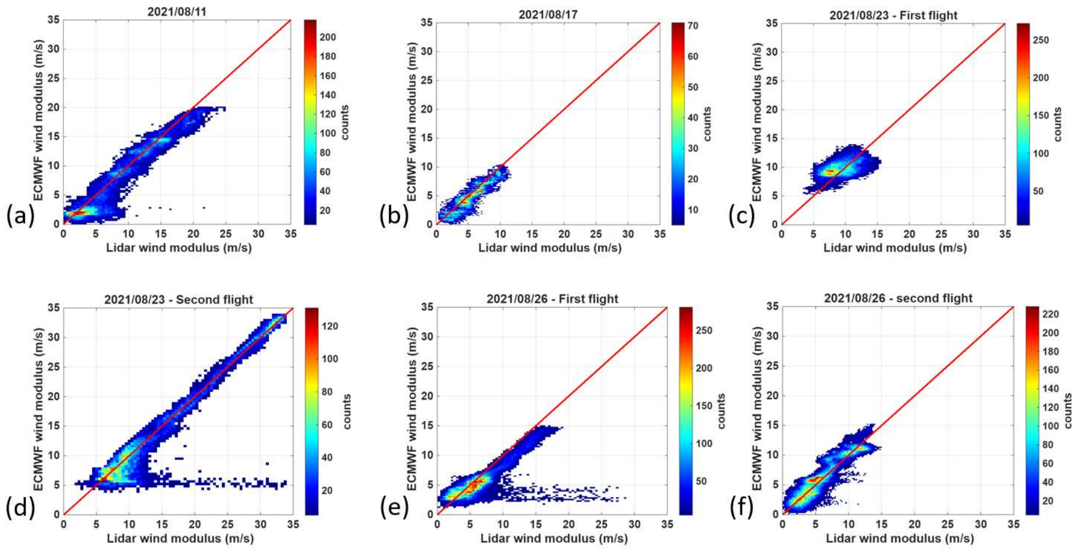

Figure 16. 2D histograms (binscatter matrices) between the lidar and ECMWF wind fields, in modulus only, for all of the flights reported in Table 5. Red lines have a zero-intercepts and slopes of one.

4. Conclusions

We have reported on the measurements performed with ONERA's airborne coherent Doppler Lidar during the Magic-2021 campaign in France and in the Arctic. More than 20 hours of lidar measurements have been realized. Vertical profiles of the horizontal wind (modulus and direction) have been obtained with 150 m vertical resolution (30 m sampling rate) and 2-4 km horizontal resolution (1.7-2.5 km sampling rate). Two wind products are made available to users and have been described: LGE-based wind profiles and FTI-based wind profiles. The FTI profiles are recommended for general use, as they are unbiased even in case of cloud cover or sea motion. Yet they exhibit, compared to LGE-based profiles, a gaussian circular excess noise vector of about 0.6 to 0.8 $m.s^{-1}$ on zonal and meridional wind components. This noise is attributed to aircraft mechanical vibrations and deformations that are not considered into the rotation matrices used for wind computation. It could be reduced by locating the aircraft navigation sensor closer to the lidar, so that both could share exactly the same framework variations during the flight. Over dry land and in clear weather conditions, LGE-based wind product would normally be the best choice, but the weather and flight conditions during the MAGIC-2021 campaign did not offer many cases where this product can be used. In principle, it could also be possible in future work to combine FTI and LGE-based wind profiles into a composite wind product, to get the best of both worlds. The lidar was able to measure vertical wind profiles with a demonstrated maximum continuous vertical range of 7.5 km without averaging, which is one of the world's best range profiling performance reported

https://doi.org/10.5194/egusphere-2026-4286
Preprint. Discussion started: 31 July 2026

so far from an airborne platform. After filtering the conical scans recorded with unsteady aircraft attitude angles and data with a too low CNR, the average data yield over six flights is about 50%. Beyond counting on better weather, this number could be improved in the future by flying more straight trajectories, by spatial and temporal data averaging (at the expense of resolution) or by upgrading the laser performance (for instance, shortening or steepening the laser pulse length would reduce lidar blind zones). The lidar measurements revealed rich details on the atmospheric aerosol structure and wind dynamics during the campaign. They have been validated by comparison with in situ radiosondes measurements, colocalized as best as possible, and found to agree within typically 1.2 m.s^{-1} in magnitude (1σ). They have also been compared with independently modelled wind fields from ECMWF ERA5 dataset. For the six flights, the lidar and modelled wind fields agree within uncertainties in the range of 1.3-2 m.s^{-1} (1σ) for both zonal and meridional wind components. All these comparisons strongly support the validity of lidar data. Actually, the lidar data may even permit in the future to identify local imperfections of wind models in weather forecast. The airborne Doppler lidar LIVE thus appears as a promising tool for future scientific campaigns dedicated to climate modelling and atmospheric dynamics.

Appendix A

As illustrated in Figure 3, the comparison between LGE-derived (Lidar Ground Echo) and FTI-derived (Flight Test instrumentation) aircraft groundspeed values shows a shift between both datasets, especially on the y and z components. This indicates some misalignment between lidar and aircraft frames of reference, that must be considered. The relationship between both sets of groundspeed data can be expressed using the following equation:

$$GS = M_{Lid2ATR}(\theta_x, \theta_y, \theta_z)\, GE + \varepsilon \qquad (A.1)$$

Where GS and GE are 3xN matrices stacking, horizontally, N groundspeed column vectors of dimension 3x1, provided respectively by FTI (in the aircraft frame of reference), and by the lidar ground-echo (in its own frame of reference). The term ε is also a 3xN matrix which accounts for the statistical deviation between the two measurements and $M_{Lid2ATR}$ is the 3x3 transition matrix from the lidar to the aircraft frame of reference, function of a set of rotation angles $\{\theta_x, \theta_y, \theta_z\}$ around roll, pitch and yaw axes respectively. For small angles, which is the case for a misalignment, the transition matrix has a linear form:

$$M_{Lid2ATR}(\theta_x, \theta_y, \theta_z) \cong \begin{bmatrix} 1 & \theta_z & -\theta_y \\ -\theta_z & 1 & \theta_x \\ \theta_y & -\theta_x & 1 \end{bmatrix} \qquad (A.2)$$

where the trigonometric convention is used for angle signs. Using a clear weather flight part over dry land (in this work, the test flight in France of 2021/08/11), it is possible to adjust the FTI-derived groundspeed GS against the LGE-derived groundspeed GE for the three vector components, and to find the transition matrix that offers the best one-to-one correspondence. For that purpose, we compute the set of angles $\{\hat{\theta}_x, \hat{\theta}_y, \hat{\theta}_z\} = \text{argmin}\left(J(\theta_x, \theta_y, \theta_z)\right)$ which minimizes the

https://doi.org/10.5194/egusphere-2026-4286
Preprint. Discussion started: 31 July 2026

distance, in a least-square sense, between both data sets expressed in the same frame of reference (the aircraft frame is chosen here). Assuming identical statistical deviations with variance σ_ε^2 for each groundspeed vector and each vector component, the criterion $J(\theta_x, \theta_y, \theta_z)$ is given by:

$$J(\theta_x,\theta_y,\theta_z) = \frac{-1}{2\sigma_\varepsilon^2}\operatorname{trace}\left(\left[GS - M_{Lid2ATR}(\theta_x,\theta_y,\theta_z)\,GE\right]\left[GS - M_{Lid2ATR}(\theta_x,\theta_y,\theta_z)\,GE\right]^t\right) \qquad (A.3)$$

$$= -\frac{(GS_x - GE_x - \theta_z GE_y + \theta_y GE_z)(GS_x - GE_x - \theta_z GE_y + \theta_y GE_z)^t}{2\sigma_\varepsilon^2}$$

$$-\frac{(GS_y + \theta_z GE_x - GE_y - \theta_x GE_z)(GS_y + \theta_z GE_x - GE_y - \theta_x GE_z)^t}{2\sigma_\varepsilon^2}$$

$$-\frac{(GS_z - \theta_y GE_x + \theta_x GE_y - GE_z)(GS_z - \theta_y GE_x + \theta_x GE_y - GE_z)^t}{2\sigma_\varepsilon^2}$$

Where the superscript *t* stands for "transposed", and the subscripts x, y or z stand for the row index (named after the spatial components) of the matrices GS and GE. The derivative of $J(\theta_x, \theta_y, \theta_z)$ relative to the angles is expected to be equal to zero for $\{\theta_x = \hat{\theta}_x, \theta_y = \hat{\theta}_y, \theta_z = \hat{\theta}_z\}$. This yields the following solution:

$$\begin{bmatrix}\hat{\theta}_x\\ \hat{\theta}_y\\ \hat{\theta}_z\end{bmatrix} = \begin{bmatrix} -GE_zGE_z^t - GE_yGE_y^t & GE_xGE_y^t & GE_xGE_z^t \\ GE_yGE_x^t & -GE_xGE_x^t - GE_zGE_z^t & GE_yGE_z^t \\ GE_zGE_x^t & GE_zGE_y^t & -GE_yGE_y^t - GE_xGE_x^t \end{bmatrix}^{-1} \begin{bmatrix} GS_zGE_y^t - GS_yGE_z^t \\ GS_xGE_z^t - GS_zGE_x^t \\ GS_yGE_x^t - GS_xGE_y^t \end{bmatrix} \qquad (A.4)$$

For the data shown in the paper, this leads numerically to $\hat{\theta}_x$ = +0.00 °, $\hat{\theta}_y$ = -0.93 °, $\hat{\theta}_z$= +3.25 °.

It is possible to have an estimation of this realignment procedure accuracy by analyzing the fit residuals data. The residuals can be expressed as the difference between the FTI and LGE groundspeed vectors expressed in the aircraft frame of reference, after applying the corrective lidar-to-aircraft rotation matrix to the LGE data. The residual matrix is equal to:

$$\begin{bmatrix}R_x\\ R_y\\ R_z\end{bmatrix} = \begin{bmatrix} GS_x - GE_x - \hat{\theta}_z GE_y + \hat{\theta}_y GE_z \\ GS_y + \hat{\theta}_z GE_x - GE_y - \hat{\theta}_x GE_z \\ GS_z - \hat{\theta}_y GE_x + \hat{\theta}_x GE_y - GE_z \end{bmatrix} \qquad (A.5)$$

From the dataset used for the alignment procedure, the set of variances $\{\sigma_{R_x}^2, \sigma_{R_y}^2, \sigma_{R_z}^2\}$ of the three components of the residuals can be computed directly. We can then refine our model of the error ε considering this set of distinct variances to weight the least-square function, instead of using a single σ_ε^2 parameter. The weighted least-square function, which, for a gaussian noise, also corresponds to the signal log-likelihood, becomes:

$$J(\theta_x,\theta_y,\theta_z) = -\frac{(GS_x - GE_x - \theta_z GE_y + \theta_y GE_z)(GS_x - GE_x - \theta_z GE_y + \theta_y GE_z)^t}{2\sigma_{R_x}^2} \qquad (A.6)$$

https://doi.org/10.5194/egusphere-2026-4286
Preprint. Discussion started: 31 July 2026

$$-\frac{\left(GS_y+\theta_z GE_x-GE_y-\theta_x GE_z\right)\left(GS_y+\theta_z GE_x-GE_y-\theta_x GE_z\right)^t}{2\sigma_{R_y}^2}$$
$$-\frac{\left(GS_z-\theta_y GE_x+\theta_x GE_y-GE_z\right)\left(GS_z-\theta_y GE_x+\theta_x GE_y-GE_z\right)^t}{2\sigma_{R_z}^2}$$

720 The Fisher information matrix (van Trees, 1997), can then be calculated, as the log-likelihood second derivatives with respect to the set of angles $\theta_x, \theta_y, \theta_z$. This leads to:

$$F=\begin{bmatrix} \frac{GE_yGE_y^t}{\sigma_{R_z}^2}+\frac{GE_zGE_z^t}{\sigma_{R_y}^2} & -\frac{GE_xGE_y^t}{\sigma_{R_z}^2} & -\frac{GE_xGE_z^t}{\sigma_{R_y}^2} \\ -\frac{GE_xGE_y^t}{\sigma_{R_z}^2} & \frac{GE_xGE_x^t}{\sigma_{R_z}^2}+\frac{GE_zGE_z^t}{\sigma_{R_x}^2} & -\frac{GE_yGE_z^t}{\sigma_{R_x}^2} \\ -\frac{GE_xGE_z^t}{\sigma_{R_y}^2} & -\frac{GE_yGE_z^t}{\sigma_{R_x}^2} & \frac{GE_xGE_x^t}{\sigma_{R_y}^2}+\frac{GE_yGE_y^t}{\sigma_{R_x}^2} \end{bmatrix} \qquad (A.7)$$

The diagonal terms of the inverse of the Fisher information matrix finally yield the Cramér-Rao lower bounds (van Trees,
725 1997) on the variance of the estimated angles $\{\hat{\theta}_x, \hat{\theta}_y, \hat{\theta}_z\}$:

$$\begin{aligned} \sigma_{\hat{\theta}_x}^2 &\geq (F^{-1})_{1,1} \\ \sigma_{\hat{\theta}_y}^2 &\geq (F^{-1})_{2,2} \\ \sigma_{\hat{\theta}_z}^2 &\geq (F^{-1})_{3,3} \end{aligned} \qquad (A.8)$$

For gaussian noise, the weighted least-square estimator is equivalent to the maximum-likelihood estimator, which is known to reach the Cramér-Rao bound at least asymptotically. Therefore, we use these bounds to obtain the angle estimation uncertainties (i.e. standard deviations) mentioned in the paper: θ_x = +0.00 ± 0.21°, θ_y = -0.93 ± 0.03°, θ_z = +3.25 ± 0.05°.

730

The following development now aims at assessing the significance of these small rotation angles, with respect to wind measurement. We want to derive the wind bias when we use the corrective lidar-to-aircraft rotation matrix, and when we do not. Let us call W a single 3x1 column vector, representing the true wind speed vector relative to the ground of a single given range gate, in the aircraft frame of reference. Air velocity $\hat{V}$ measured by lidar, in its own frame of reference, is thus the
735 composition of this true wind speed W relative to ground and the groundspeed vector GS relative to aircraft. We neglect here the random noise ε (considered as a zero-mean process), in order to focus on the bias calculation. $\hat{V}$ can be expressed as:

$$\hat{V}=M_{Lid2ATR}^{-1}\left(\theta_x,\theta_y,\theta_z\right)(W+GS) \qquad (A.9)$$

Where $M_{Lid2ATR}$ is the lidar-to-aircraft rotation matrix, and θ_x, θ_y, θ_z the true rotation angles between the aircraft and lidar frames, due to misalignment. Conversely, the lidar signal processing yields the estimated wind vector speed $\hat{W}$ using the
740 following relation:

https://doi.org/10.5194/egusphere-2026-4286
Preprint. Discussion started: 31 July 2026

$$\widehat{W} = M_{Lid2A}\ \ (\hat{\theta}_x, \hat{\theta}_y, \hat{\theta}_z)\hat{V} - GS \tag{A.10}$$

where $\hat{\theta}_x, \hat{\theta}_y, \hat{\theta}_z$ are the estimated angles (obtained above) of the lidar-to-aircraft rotation matrix. Thus, the equation linking the estimated wind vector $\widehat{W}$ with the true wind vector W is given by:

$$\widehat{W} = M_{Lid2ATR}(\hat{\theta}_x, \hat{\theta}_y, \hat{\theta}_z)M_{Lid2ATR}^{-1}(\theta_x, \theta_y, \theta_z)(W + GS) - GS \tag{A.11}$$

Since the modulus of $\widehat{W}$ is bounded by the sum of the modulus of its sub terms, it can be written that:

$$\|\widehat{W}\| \leq \|M_{Lid2ATR}(\hat{\theta}_x, \hat{\theta}_y, \hat{\theta}_z)M_{Lid2A}^{-1}\ \ (\theta_x, \theta_y, \theta_z)W\| + \left\|\left(I - M_{Lid2ATR}(\hat{\theta}_x, \hat{\theta}_y, \hat{\theta}_z)M_{Lid2ATR}^{-1}(\theta_x, \theta_y, \theta_z)\right)GS\right\| \tag{A.12}$$

Because $M_{Lid2ATR}$ is a rotation matrix, it represents an isometry transformation that does not change the modulus of the vector to which it is applied. This is also true for products of rotation matrices. The first term of the right-hand side can thus be simplified (the second cannot because $(I - M_{Lid2ATR}M_{Lid2A}^{-1}\ \ )$ is not an isometry). We obtain:

$$\|\widehat{W}\| \leq \|W\| + \left\|\left(I - M_{Li}\ \ \ \ (\hat{\theta}_x, \hat{\theta}_y, \hat{\theta}_z)M_{Lid2A}^{-1}\ \ (\theta_x, \theta_y, \theta_z)\right)GS\right\| \tag{A.13}$$

The wind modulus bias $b = \|\widehat{W}\| - \|W\|$ then appears, and it is bounded as following:

$$b \leq \left\|\left(I - M_{Lid2ATR}(\hat{\theta}_x, \hat{\theta}_y, \hat{\theta}_z)M_{Lid2ATR}^{-1}(\theta_x, \theta_y, \theta_z)\right)GS\right\| \tag{A.14}$$

Assuming small angular misalignment values, we have:

$$I - M_{Lid2A}\ \ (\hat{\theta}_x, \hat{\theta}_y, \hat{\theta}_z)M_{Lid2ATR}^{-1}(\theta_x, \theta_y, \theta_z) \cong \begin{bmatrix} 0 & \theta_z - \hat{\theta}_z & \hat{\theta}_y - \theta_y \\ \hat{\theta}_z - \theta_z & 0 & \theta_x - \hat{\theta}_x \\ \theta_y - \hat{\theta}_y & \hat{\theta}_x - \theta_x & 0 \end{bmatrix} \tag{A.15}$$

Reporting A.15 into A.14, the full expression of bias bound can be computed directly. We shall only write here a simplified form for it, assuming that the aircraft is flying at constant flight altitude (GS_z=0) and with negligible crosswind compared to the total groundspeed ($GS_y \approx 0$). We then obtain:

$$\mathrm{b} \leq GS_x\left((\hat{\theta}_y - \theta_y)^2 + (\hat{\theta}_z - \theta_z)^2\right)^{\frac{1}{2}} \tag{A.16}$$

If one neglects to estimate the small lidar-to-aircraft frame misalignment, that means that $\hat{\theta}_y$ and $\hat{\theta}_z$ are both assumed to be zero (while they are not). The maximum modulus bias in this case is:

$$b_{max}{=}GS_x\left(\theta_y^2 + \theta_z^2\right)^{\frac{1}{2}} \tag{A.17}$$

For an aircraft flying at the average cruise speed GS_x=100 m.s^{-1}, and considering the true misalignment angles derived before, the maximum bias is as high as 5.9 m.s^{-1}. If the misalignment angles are estimated, it is still possible to have some measurement bias, because the estimation has a limited accuracy. A measure of the potential residual bias can be obtained by replacing the true misalignment angles in the preceding formula by the standard deviations of their respective estimates, i.e.:

$$b_{max}{=}GS_x\left(\sigma_{\hat{\theta}_y}^2 + \sigma_{\hat{\theta}_z}^2\right)^{\frac{1}{2}} \tag{A.18}$$

In this case, we obtain a maximum potential bias of 0.1 m.s^{-1}, which indicates a very efficient bias mitigation. It can therefore be concluded that the lidar-to-aircraft frame misalignment correction is essential for horizontal wind measurements, and that the procedure described in this paper is accurate enough to avoid systematic bias at the scale of a full flight.

The rationale presented above holds for the FTI-based wind products. For the LGE-based product, it is straightforward to follow the same steps to derive the bias that would be obtained if the lidar-to-aircraft transition matrix was not used. Assuming a simple case where the wind has mainly an x-axis projection in the aircraft frame, we obtain:

$$b_{max,LGE} = W_x\left(\theta_y^2 + \theta_z^2\right)^{\frac{1}{2}} \qquad (A.19)$$

In the planetary boundary layer, the wind magnitude is in the typical magnitude of 10 m.s^{-1} or less, which implies a much lower potential bias if the transition matrix is not applied (<0.6 m.s^{-1}). However, winds can be much stronger higher at the aircraft flight altitude. It is therefore wise to use the transition matrix even for the LGE-based wind product.

Data availability: Data can be downloaded in NetCDF format from AERIS website: https://magic.aeris-data.fr/magic2021. They can be used freely as long as users comply with AERIS data policy. LIVE data must be referred to by the following citation: "Valla, M. Cézard, N. & Crevoisier, C. (2026). Live Lidar-L3-MAGIC-2021 [dataset]. Aeris. https://doi.org/10.25326/866"

Author contributions. NC and MV performed the analysis and provided the draft of the manuscript. NC, MV and LL performed the airborne measurements. MV, BA, JL, WPR, DG, and CP led the lidar development and aircraft integration phase. MV ADB and LL developed the core algorithms for wind speed retrieval. AD, FG, and AL led the laser development and integration into the lidar, MQ provided the ECMWF wind fields for this study, EW performed the data comparison between LIVE, radiosondes and ATR-42 Pitot tube, CC led the MAGIC-2021 campaign. All co-authors reviewed the paper.

Competing interests: the authors have no competing interests to declare.

Acknowledgements: the MAGIC-2021 campaign was led by CNRS-LMD and CNES, supported by ESA and EUMETSAT. We are grateful for their leadership. We also express our gratitude to DLR and SAFIRE members, with whom we had the pleasure to work and fly. Plots with GoogleEarth backgrounds have been realized using the Matlab *KML Toolbox*© from R.Fernandes de Oliveira. We are grateful to the author for sharing this tool.

Financial support: Lidar LIVE is part of TERRISCOPE, a shared research platform in airborne optical remote sensing co-funded by the European Union (ERDF), Occitanie French region, ONERA, SOFRADIR, BOREAL, LEOSPHERE (now VAISALA) and M3 SYSTEMS. The MAGIC-2021 campaign was funded by CNES (APR2021), ESA (MAGIC4AMPAC

https://doi.org/10.5194/egusphere-2026-4286
Preprint. Discussion started: 31 July 2026

project) and EUMETSAT. ONERA members were supported by ONERA Scientific Direction within the Research Project MIEL, and by CNES under APR contract n°4500070182.

References

Amediek, A., Ehret, G., Fix, A., Wirth, M., Büdenbender, C., Quatrevalet, M., Kiemle, C., and Gerbig, C.: CHARM-F, a new airborne integrated-path differential-absorption lidar for carbon dioxide and methane observations: measurement performance and quantification of strong point source emissions, Appl. Opt., 56, 5182-5197, https://doi.org/10.1364/AO.56.005182, 2017.

Augere, B., Valla, M., Durecu, A., Dolfi-Bouteyre, A., Goular, D., Gustave, F., Planchat, C., Fleury, D., Huet, T., and Besson, C.: Three-Dimensional Wind Measurements with the Fibered Airborne Coherent Doppler Wind Lidar LIVE, Atmosphere, 10, 549, doi:10.3390/atmos10090549, 2019.

Browning, K. A. and Wexler R.: The determination of kinematic properties of a wind field using Doppler radar. J. Appl. Meteor., 7, 105–113, https://doi.org/10.1175/1520-0450(1968)007<0105:tdokpo>2.0.co;2, 1968.

C3S-CDS, Copernicus Climate Change Service, Climate Data Store: ERA5 post-processed daily-statistics on single levels from 1940 to present. Copernicus Climate Change Service (C3S) Climate Data Store (CDS). doi: 10.24381/cds.4991cf48, 2024.

Cézard, N., Valla, M., Lombard, L., Goular, D., Augère, B., Dolfi-Bouteyre, A., Fix, A., Quatrevalet, M., Bès, C., and Crevoisier, C.: Double-Lidar airborne mission over Scandinavia for atmospheric transport assessment of CH4 and CO2. ILRC-30 - International Laser Radar Conference, Online, United States. pp.S07_O03, https://hal.science/hal-03769242v1, 2022.

Crevoisier, C.: The MAGIC initiative, https://magic.aeris-data.fr/, last access: 20 July 2026, 2018.

Crevoisier, C.: MAGIC2021 Logbook, https://magic.aeris-data.fr/magic2021/, last access: 20 July 2026, 2021.

Fujii, T., and Fukuchi, T. (Eds. Taylor & Francis Group): Laser Remote Sensing, 912 pp, 2005.

GCOS, The 2022 GCOS Implementation Plan (GCOS-244), https://library.wmo.int/idurl/4/58104, last access: 20 July 2026, 2022.

Jain, P., Sharma, A.R., Acuna, D.C., Abatzoglou, J.T., and Flannigan, M.: Record-breaking fire weather in North America in 2021 was initiated by the Pacific northwest heat dome. Commun. Earth Environ. 5, 202. https://doi.org/10.1038/s43247-024-01346-2, 2024.

Kavaya, M.J., Beyon, J.Y., Koch, G.J., Petros, M., Petzar, P.J., Singh, U.N., Trieu, B.C., and Yu, J.: The Doppler aerosol wind (DAWN) airborne, wind-profiling coherent-detection lidar system: overview and preliminary flight results, J. Atmos. Ocean. Technol. 31, 826–842, https://doi.org/10.1175/JTECH-D-12-00274.1, 2014.

Krautwurst, S., Fruck, C., Wolff, S., Borchardt, J., Huhs, O., Gerilowski, K., Gałkowski, M., Kiemle, C., Quatrevalet, M., Wirth, M., Mallaun, C., Burrows, J. P., Gerbig, C., Fix, A., Bösch, H., and Bovensmann, H.: Identification and quantification

https://doi.org/10.5194/egusphere-2026-4286
Preprint. Discussion started: 31 July 2026

of CH4 emissions from Madrid landfills using airborne imaging spectrometry and greenhouse gas lidar, Atmos. Chem. Phys., 25, 14669–14702, https://doi.org/10.5194/acp-25-14669-2025, 2025.

Langot, F., Crevoisier, C., Lauvaux, T., Abdallah, C., Pernin, J., Lin, X., Saunois, M., Guedj, A., Ponthieu, T., Moyé, J., Ramonet, M., Roiger, A., Gottschaldt, K.-D., and Fiehn, A.: Evaluating Weather and Chemical Transport Models at High Latitudes using MAGIC2021 Airborne Measurements. Atmos. Meas. Tech., 18, 5955–5983, https://doi.org/10.5194/amt-18-5955-2025, 2025.

Liu, J., Zhu, X., Diao, W., Zhang, X., Liu, Y., Bi, D., Jiang, L., Shi, W., Zhu, X., and Chen, W.: All-fiber airborne coherent Doppler lidar to measure wind profiles, in: The 27th International Laser Radar Conference (ILRC 27), New York City, NY, USA, https://doi.org/10.1051/epjconf/201611910002, 2016.

Popovicheva, O., Kobelev, V., Chichaeva, M., and Kasimov, N.: Unprecedented wildfire smoke in the Siberian Arctic in August 2021, EGU General Assembly 2022, Vienna, Austria, 23–27 May 2022, EGU22-9775, https://doi.org/10.5194/egusphere-egu22-9775, 2022.

Schäfler, A., Dörnbrack, A., Kiemle, C., Rahm, S., and Wirth, M.: Tropospheric Water Vapor Transport as Determined from Airborne Lidar Measurements. J. Atmos. Oceanic Technol., 27, 2017–2030, https://doi.org/10.1175/2010JTECHA1418.1, 2010.

Schäfler, A., Harvey, B., Methven, J., Doyle, J. D., Rahm, S., Reitebuch, O., Weiler, F. and Witschas B.: Observation of Jet Stream Winds during NAWDEX and Characterization of Systematic Meteorological Analysis Errors. Mon. Wea. Rev., 148, 2889–2907, https://doi.org/10.1175/MWR-D-19-0229.1, 2020.

Schroeder, P., Brewer, W.A., Choukulkar, A., Weickmann, A., Zucker, M., Holloway, M. W., and Sandberg, S.: A compact, flexible, and robust micropulsed Doppler lidar, J. Atmos. Ocean. Technol. 37, 1387–1402, https://doi.org/ 10.1175/JTECH-D-19-0142.1, 2020.

SRTM30: https://icesat.gsfc.nasa.gov/icesat/tools/SRTM30_Documentation.html, last access: 20 July 2026.

Stengel R.F.: Flight Dynamics, Princeton University Press, https://doi.org/10.1515/9781400866816, 2005.

Smalikho, I.: Techniques of wind vector estimation from data measured with a scanning coherent Doppler lidar. J. Atmos. Ocean. Technol, 20, 276–291, https://doi.org/10.1175/1520-0426(2003)020<0276:TOWVEF>2.0.CO;2, 2003.

van Trees, H.L. (Eds. Wiley): Detection, Estimation, and Modulation Theory, 1997.

Weissmann, M., Busen, R., Dörnbrack, A., Rahm, S., and Reitebuch, O.: Targeted observations with an airborne wind lidar, J. Atmos. Ocean. Tech., 22, 1706–1719, https://doi.org/10.1175/JTECH1801.1, 2005.

Witschas, B., Lemmerz, C., Geiß, A., Lux, O., Marksteiner, U., Rahm, S., Reitebuch, O., and Weiler, F.: First validation of Aeolus wind observations by airborne Doppler wind lidar measurements, Atmos. Meas. Tech., 13, 2381–2396, https://doi.org/10.5194/amt-13-2381-2020, 2020.

https://doi.org/10.5194/egusphere-2026-4286
Preprint. Discussion started: 31 July 2026

Witschas, B., Rahm, S., Dörnbrack, A., Wagner, J., Rapp, M.: Airborne wind lidar measurements of vertical and horizontal winds for the investigation of orographically induced gravity waves, J. Atmos. Ocean. Technol. 34, 1371–1386, https://doi.org/10.1175/JTECH-D-17-0021.1, 2017.

Wolff, S., Ehret, G., Kiemle, C., Amediek, A., Quatrevalet, M., Wirth, M., and Fix, A.: Determination of the emission rates of CO2 point sources with airborne lidar, Atmos. Meas. Tech., 14, 2717–2736, https://doi.org/10.5194/amt-14-2717-2021, 2021.

Yew, R.L., Johnson, B. C., Gibson, B. C., and Mohamed A.: A review of airborne Doppler lidar for wind-sensing, Progress in Aerospace Sciences, 157, 101127, ISSN 0376-0421, https://doi.org/10.1016/j.paerosci.2025.101127, 2025.

Zhang, X., Lin, Z., Gao, C., Han, C., Fan, L. and Zhao, X.: Evaluation and wind field detection of airborne Doppler wind lidar with automatic intelligent processing in north China, Atmosphere 15, 536, https://doi.org/10.3390/atmos15050536, 2024.